minerals

MDPI

Article

Permo-Triassic Clastic Rocks from the Ghomaride Complex and Federico Units (Rif Cordillera, N Morocco): An Example of Diagenetic-Metamorphic Transition

Mª Dolores Rodríguez-Ruiz [1,*], Isabel Abad [2] and María J. Bentabol [1]

[1] Departamento de Química Inorgánica, Cristalografía y Mineralogía, Universidad de Málaga, 29071 Málaga, Spain; bentabol@uma.es

[2] Departamento de Geología and CEACTierra, Universidad de Jaén, Campus Las Lagunillas s/n, 23071 Jaén, Spain; miabad@ujaen.es

* Correspondence: mdrodriguez@uma.es; Tel.: +34-636373300

Received: 26 September 2019; Accepted: 22 November 2019; Published: 29 November 2019

Abstract: A detailed characterization of the mineralogy corresponding to the low-grade diagenetic-metamorphic sequence of the clastic rocks from the Beni Mezala antiform has allowed the processes implied in their origin to be stablished, integrating them in the geodynamic evolution of the Rif-Betic mountain range during the Alpine orogeny. A progressive evolution towards chemical and textural equilibrium was observed. The illite "crystallinity" (CIS) ranges from diagenetic-lower anchizone in Ghomaride complex (CIS: 1.50–0.37 Δ°2θ) to epizone in the deepest Federico units (CIS: 0.29–0.21 Δ°2θ). The main phyllosilicates in the diagenetic samples are illite ($2M_1$-1*M* polytypes) and kaolinite, with mixed-layer illite/smectite and chlorite, but the mixed layers disappear in the lower anchizone samples, which show sudoite and dickite. Pyrophyllite is also present in the upper anchizone (0.43–0.29 Δ°2θ) whereas the epizone samples show muscovite ($2M_1$-3*T* polytypes), chlorite, paragonite, and intermediate micas. The chlorite geothermometers give a *T* range of 150 to 400 °C, and the *b* parameter of $2M_1$ micas (8.992–9.029 Å) indicates low to intermediate pressure regional metamorphism (1–3 kbar) although the wide range of phengitic substitution in micas and the 3*T* polytype suggest a wider pressure range in coherence with the clockwise PTt evolution for the Rif Cordillera during the Alpine orogeny.

Keywords: anchizone; Ghomaride; illite "crystallinity"; phyllite; phyllosilicates; polytype; quartzite; SEM/TEM; sandstones; semi-empirical thermometry

1. Introduction

The establishment of metamorphic paths in very low- and low-grade metamorphic stratigraphic sequences of clastic rocks is not an easy task as textural relations among minerals are not obvious; intergrowths of phases, a general lack of equilibrium, and changes in the mineral paragenesis are characteristic below the biotite isograd [1–5]. For these reasons, researchers have relied on criteria, such as polytypism, crystallite size values, or chemical characterization of the metastable sheet silicates, that are only qualitative indicators of the stages the phyllosilicates have reached through a series of metastable mineral reactions during low-temperature metamorphism [6]. This situation emphasizes the notion of reaction progress: Metastable phyllosilicates undergoing reactions towards the state of stable chemical and textural equilibrium reached in greenschist-facies rocks [7,8]. According to Árkai [9], two progressive trends of phyllosilicate crystal-chemical changes occur between early diagenesis and epizone in pelitic sequences: dioctahedral smectite–illite/smectite

interstratified clay mineral–illite–dioctahedral K-rich white mica (muscovite) and trioctahedral smectite–corrensite/smectite interstratified clay mineral–chlorite/corrensite–chlorite. There is another dioctahedral series that evolves from kaolinite towards pyrophyllite, but details about this series are currently sparse in metapelitic rocks, being much more abundant in coarse-grain rocks ([10] and references therein). In addition, the data derived from the application of different geothermometric methods, under these metamorphic conditions, may also contribute to the knowledge of the pressure (*P*)–temperature (*T*) paths and their tectonic significance [11,12].

The aim of this contribution was to characterize the low-grade metamorphism in the Ghomaride complex and Federico units from the higher units of the Internal Zone of the Rif Cordillera (N Morocco) in order to establish the *T* and *P* conditions reached by these metasediments and improve the interpretation of their tectonometamorphic evolution. For this purpose, a multiproxy approach was applied, including X-ray diffraction (XRD) measurements, textural and chemical characterization of mineral phases by scanning electron microscopy (SEM), and thermometric calculations. The XRD determinations include the measuring of the crystal-chemical parameters: The *b* cell parameter [13] and the illite "crystallinity" of white micas [14]. The dataset provided here is an example of how knowledge of crystal-chemical parameters of phyllosilicate minerals contributes to the understanding of the evolution of an orogen. For the thermometric calculations, semi-empirical approaches based on the chlorite compositions [15,16] were used. Finally, the very fine-grained texture of these rocks, in some cases, made it necessary to examine them not only by petrographic and scanning electron microscopy but also by transmission electron microscopy (TEM). Therefore, this research aimed to establish the prograde and retrograde processes responsible for the low-grade mineral assemblages and their textural characteristics from the crystal-chemical parameters, compositions, and textural relationships up to lattice scale of phyllosilicates. In addition, there is little knowledge of the effect of more coarse-grained lithologies on the mineralogical changes during very low-grade metamorphism, and in the studied area, clastic rocks with different grain sizes were sampled, from phyllites to sandstones. Lastly, we tried to correlate all these data with the geodynamic evolution of the Rif Cordillera during the Alpine orogeny. This type of study has been previously applied to the metamorphic evolution in the equivalent Betic Cordillera units, on the other side of the Gibraltar Strait ([17–20]; among others). Meanwhile, many authors have studied the Moroccan and southernmost part of the Betic-Rif orogen in the last decades (e.g., [21–29]) although mainly from a structural, geodynamic, lithostratigraphic, palaeostratigraphic, and palaeogeographic point of view.

2. Geological Setting and Materials

The Rif and Betic chains, at the south and north of the Alboran Sea, respectively, form an arc-shaped mountain belt around the Strait of Gibraltar as a consequence of the convergence between Africa and Iberia during late Mesozoic to Cenozoic. They both represent the westernmost peri-Mediterranean alpine chains (Figure 1) and are characterized by the Internal and External Zones, Flyschs domain, and Neogene basins (Figure 1b). The Internal Zone comprises two tectonic complexes in the Rif Cordillera: the Sebtide at the bottom and the Ghomaride at the top (so-called Alpujárride and Maláguide, respectively, in the Betic Cordillera) (Figure 2a). The geometric relationship between them is practically constant, with the Ghomaride complex tectonically overlying the Sebtide complex except for some locations due to local and later thrusts. The differentiation of the Ghomaride and Sebtide complexes is commonly based on variations in lithology and metamorphic grade. In the Ghomaride complex, Triassic rocks include red conglomerates, sandstones, and lutites, all displaying diagenetic conditions [30–34], and also carbonates at the end of the sequence. In contrast, the Permo-Triassic rocks of the underlying tectonic nappe (Sebtide) mainly include schists, phyllites with quarzitic intercalations, and marbles, reflecting incipient-to-advanced metamorphic conditions [22,30,34–36]. In addition, the presence of intermediate units between these two complexes has been alternatively considered as upper Sebtide units ([22,30,36,37] and references therein) or as units intermediate between the Ghomaride and Sebtide complexes ([33] and references therein). According to Kornprobst [30], these units have

been pointed out several places with the name of Federico units, with the denomination followed in this article.

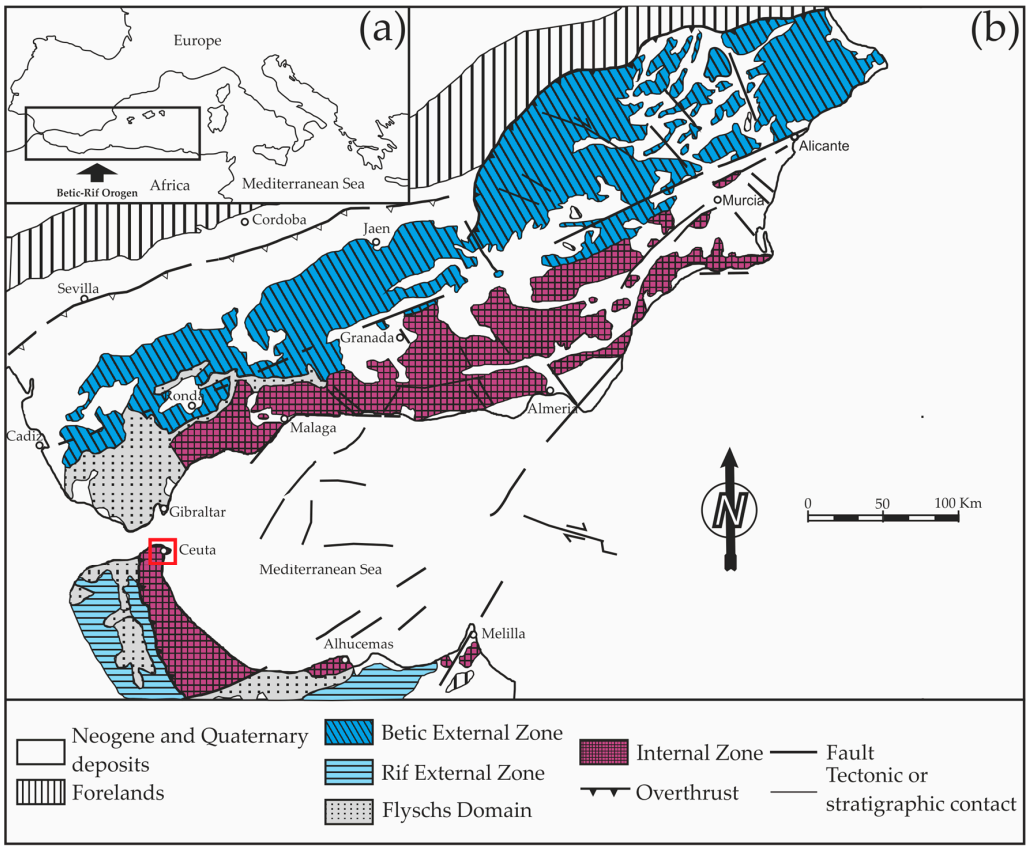

Figure 1. Geological map of the Betic-Rif Cordillera: (**a**) location of the orogen in the Mediterranean Sea; (**b**) distribution of the Internal and External Zones, Flyschs and Neogene basins of the Betic-Rif Cordillera, and location of the study area (red square) (modified from Sanz de Galdeano [38]).

The samples described in this work belong to the Permo-Triassic materials of the Ghomaride complex and Federico units. The sector where ghomaride and federico materials were sampled is the area between Ceuta and Fnideq (Figure 2). Several tectonic units have been differentiated in this location, which are, from top to bottom: Beni Hozmar, Koudiat Tiziane, and Aakaili (with clear ghomaride affinity; [30,34,35]) and Tizgarine, Boquete Anjera, Beni Mezala 2, and Beni Mezala 1 (Federico units, [30]) (Figure 2b). The three ghomaride units are formed by the same stratigraphic sequence of materials: Paleozoic phyllites, limestones, conglomerates and greywackes, Triassic conglomerates, sandstones, and lutites, with some carbonate intercalations in the middle Triassic and also carbonates at the end of the Triassic, passing to the Jurassic (Figure 3). With respect to the Federico units, all of them show similar stratigraphic sequences: Carboniferous metagreywackes and dark phyllites at the bottom, and Permo-Triassic metapelites and conglomerates and Triassic quartzites and carbonates at the top, as can be seen in Figure 3. According to Sanz de Galdeano et al. [33], the stratigraphic Triassic sequences from the Federico units have intermediate characteristics (the existence or not of levels of conglomerates, the presence of pelites or metapelites and specially the development of carbonates) in relation to the Triassic successions of the sebtide and ghomaride units. The transition from the upper unit (Tizgarine) to the lower units is marked by a change in color from red to blue and an increase in metamorphic grade, which was recognized earlier by Milliard [39].

A total of 46 samples of Permo-Triassic clastic rocks were taken, 17 from the Ghomaride complex and 29 from the Federico units (Tables 1 and 2). During the sampling, the outer surficial material was removed to avoid any contamination by surface weathering.

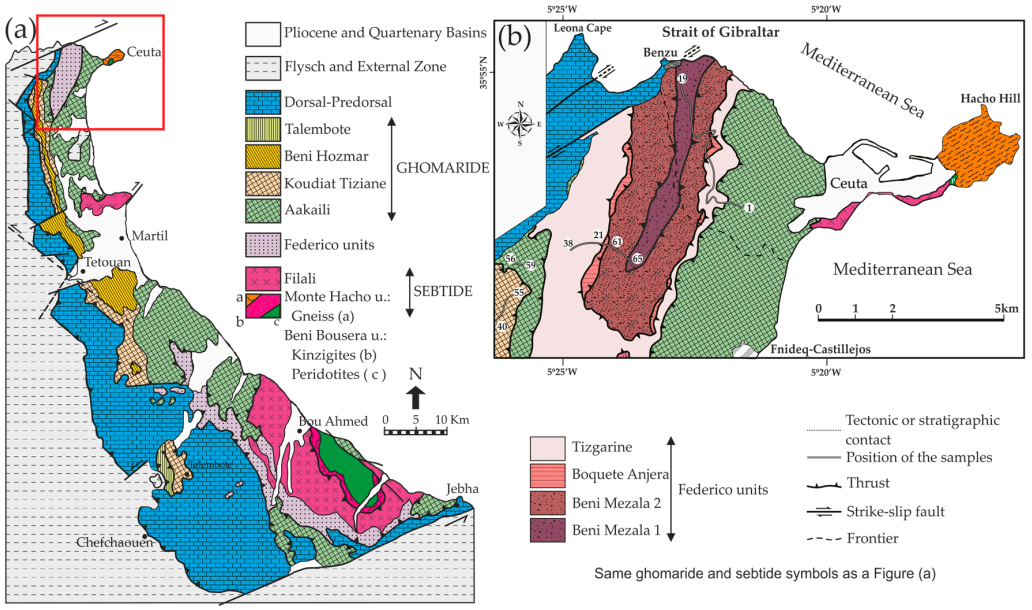

Figure 2. (**a**) Geological map of the Rif Cordillera between Ceuta and Jebhá with location of the study area (modified from Chalouan and Michard [21], and El Adraoul et al. [40]); (**b**) detailed geological sketch map of the studied area (modified from Kornprobst [30] and Kornprobst and Durand-Delga [41]). Numbers represent the range of samples taken in each of the itineraries. The Beni Hozmar unit does not appear in the figure (**b**). Samples from this unit were taken 2.5 km southwest of sample MG-40, on the national road between Fnideq and Dradia.

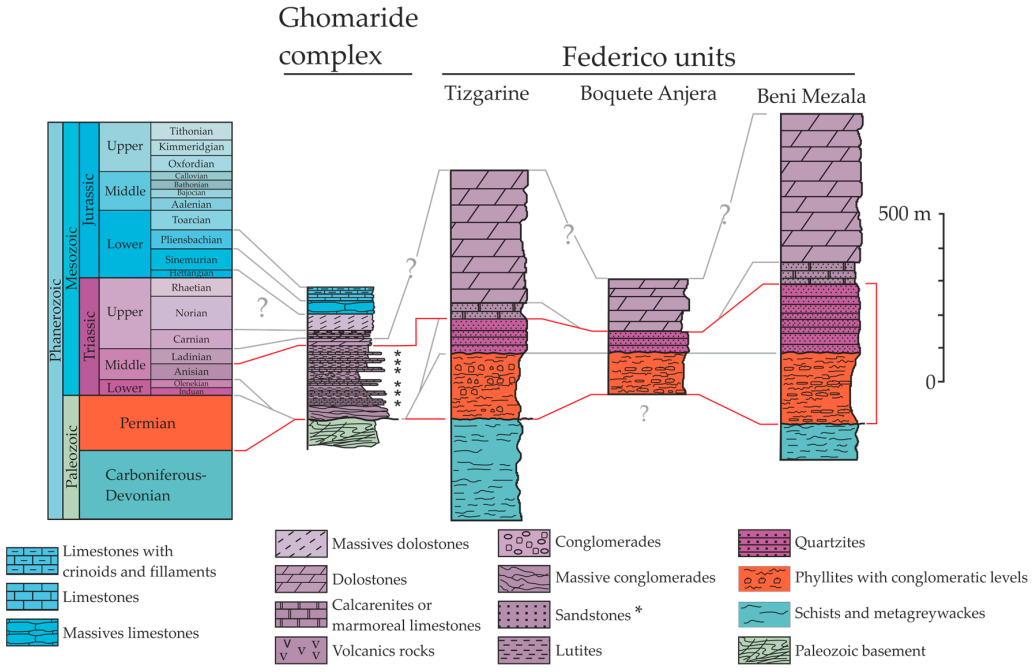

Figure 3. Stratigraphic columns corresponding to the Ghomaride complex and Federico units. Sandstones position is marked by asterisks in the Ghomaride complex. The Permo-Triassic clastic rocks of the Ghomaride complex and Federico units described in this work are included between the red lines.

Table 1. Lithology, mineralogy, CIS (Crystallinity index standard) values (Δ°2θ), polytypes, and *b* parameter (Å) of illites from the studied samples in the Ghomaride complex. Mineral abbreviations according to Whitney and Evans [42]. In addition, Na-K: Na-K intermediate white mica, I/S: mixed layer illite/smectite. n.d.: non-determined. In bold, samples studied by HRTEM.

Samples	Lithology	Mineral Assemblage	CIS	CIS EG	Polytype	*b* (Å)
Beni Hozmar unit						
BH-1	Red sandstone	Qz, Kfs, Pl, Hem, Ilt, Kln, I/S	1.50	0.75	$2M_1$–$1M$	n.d.
BH-2	Light sandstone	Qz, Kfs, Ilt, Kln	0.62	0.56	$2M_1$–$1M$	n.d.
BH-3	Red sandstone	Qz, Kfs, Hem, Ilt, Kln, Chl, I/S	0.77	0.53		n.d.
Koudiat Tiziane unit						
MG-40	Light sandstone	Qz, Kfs, Pl, Ilt, Chl	0.37	0.43	$2M_1$–$1M$	n.d.
MG-41	Red sandstone	Qz, Kfs, Hem, Ilt	n.d.	n.d.		n.d.
MG-42	Red sandstone	Qz, Kfs, Hem, Ilt, Kln	0.58	0.53		n.d.
MG-43	Light sandstone	Qz, Kfs, Ilt	0.80	0.85		n.d.
MG-44	Red lutite	Qz, Kfs, Pl, Hem, Ilt, Chl	0.65	0.59		9.0162
MG-45	Red sandstone	Qz, Kfs, Hem, Ilt	1.13	1.11		9.0096
MG-46	Red sandstone	Qz, Kfs, Pl, Dol, Hem, Ilt, Chl	0.92	0.83	$2M_1$–$1M$	9.0096
MG-47	Red sandstone	Qz, Kfs, Pl, Dol, Hem, Ilt, Chl, Kln	0.92	0.80	$2M_1$–$1M$	9.0072
MG-48	Red siltite	Qz, Kfs, Pl, Hem, Ilt, Kln, Dck, Sud	0.46	0.47	$2M_1$–$1M$	8.9916
MG-49	Purple-red sandstone	Qz, Kfs, Pl, Hem, Ilt, Chl, Kln, Dck, Sud	0.47	0.43	$2M_1$	9.0024
MG-50	Purple-red sandstone	Qz, Kfs, Pl, Hem, Ilt, Chl, Kln, Dck, Sud	0.51	0.47	$2M_1$	9.0006
MG-51	Purple-red sandstone	Qz, Kfs, Pl, Cal, Hem, Ilt, Chl, Dck, Sud	0.51	0.47	$2M_1$	9.0006
Aakaili unit						
MG-56	Purple-red sandstone	Qz, Kfs, Pl, Hem, Ilt, Na-K, Dck, Sud	0.64	0.51	$2M_1$	n.d.
MG-57	Purple-red lutite	Qz, Kfs, Pl, Hem, Ilt, Na-K, Dck, Sud	0.85	0.82	$2M_1$	8.9958

Table 2. Lithology, mineralogy, CIS values (Δ°2θ), polytypes, and *b* parameter (Å) of illites from the studied samples in the Federico units. Mineral abbreviations according to Whitney and Evans [42]. In addition, Na-K: Na-K intermediate white mica, C/V: mixed-layers chlorite/vermiculite. n.d.: non-determined. In bold, samples studied by HRTEM.

Samples	Lithology	Mineral Assemblage	CIS	CIS EG	Polytype	*b* $2M_1$	*b* $3T$
Tizgarine unit							
MG-38	Pink sandstone	Qz, Kfs, Pl, Hem, Ilt, Na-K, Chl	0.29	0.31	$2M_1$	8.9982	
MG-37	Purple-red phyllite	Qz, Kfs, Pl, Hem, Ilt, Dck, Prl, Sud	0.39	0.43	$2M_1$	8.9922	
MG-35	Purple-red phyllite	Qz, Kfs, Pl, Hem, Ilt, Prl, Chl	0.43	0.47	$2M_1$	8.9892	
MG-34	Yellow sandstone	Qz, Kfs, Pl, Ilt, Dck, Prl	0.35	0.39	$2M_1$	8.9982	
Boquete Anjera unit							
MG-23f	Purple phyllite	Qz, Kfs, Pl, Hem, Ms, Pg, Na-K, Chl	n.d.		$2M_1$	8.9868	
MG-22	Green phyllite	Qz, Kfs, Pl, Ms, Na-K, Pg, Chl	0.37	0.38	$2M_1$	9.0006	
MG-21	Purple phyllite	Qz, Kfs, Pl, Hem, Ms, Na-K, Pg, Chl	0.29	0.30	$2M_1$	9.0072	
MG-11	Smoke blue phyllite	Qz, Kfs, Hem, Ms, Chl	0.22	0.21	$2M_1$–$3T$	9.0116	9.0475
MG-11′	White quartzite	Qz, Kfs, Ms, Chl	0.21	0.21	$2M_1$–$3T$	9.0114	9.0498
MG-7	White quartzite	Qz, Kfs, Ms, Chl	0.21	0.21	$2M_1$–$3T$	n.d.	n.d.
MG-8	Blue phyllite	Qz, Kfs, Ms, Chl	0.21	0.21	$2M_1$–$3T$	9.0138	9.0474
MG-9	Blue phyllite	Qz, Kfs, Hem, Ms, Chl	0.21	n.d.	$2M_1$–$3T$	9.0162	9.0384
MG-10	Smoke blue phyllite	Qz, Kfs, Hem, Ms, Chl	0.22	0.20	$2M_1$–$3T$	9.0228	9.0474
Beni Mezala 2 unit							
MG-61	White quartzite	Qz, Kfs, Dol, Ms	0.22	0.23	$2M_1$–$3T$	9.0228	9.0498
MG-62	Smoke blue phyllite	Qz, Kfs, Hem, Ms, Chl, (C/V)	0.23	0.23	$2M_1$–$3T$	9.0228	9.0546
Beni Mezala 1 unit							
MG-19	Yellow quartzite	Qz, Kfs, Pl, Ms	0.25	0.25	$2M_1$	9.0114	
MG-18	Whitish schist	Qz, Kfs, Pl, Hem, Ms, Tlc, Vrm, C/V, Kln	0.24	0.25	$2M_1$	9.0360	
MG-18′	Whitish quartzite	Qz, Kfs, Pl, Hem, Ms, Chl	0.29	0.26	$2M_1$	9.0228	
MG-17	Dark blue phyllite	Qz, Kfs, Hem, Ms, Chl	0.23	0.22	$2M_1$–$3T$	9.0072	9.0432
MG-16	Dark blue phyllite	Qz, Kfs, Hem, Ms, Pg, Chl	0.22	0.23	$2M_1$	9.0096	
MG-15	Dark blue phyllite	Qz, Kfs, Pl, Hem, Ms, Na-K, Pg, Chl	0.27	0.28	$2M_1$	9.0138	
MG-14	Dark blue phyllite	Qz, Pl, Hem, Ms, Na-K, Na-Ca, Pg, Prl, Chl	0.27	0.27	$2M_1$	8.9934	
MG-13	Dark blue phyllite	Qz, Kfs, Pl, Hem, Ms, Na-K, Pg, Chl	0.31	0.31	$2M_1$	9.0024	
RMG-13Df	Dark blue phyllite	Qz, Pl, Pmp, Ep, Ms, Vrm	n.d.		$2M_1$	9.0036	
RMG-13Af	Dark blue phyllite	Qz, Kfs, Pl, Hem, Ms, Pg, Na-K, Chl	n.d.		$2M_1$	9.0006	
MG-12	Quarzite	Qz, Kfs, Ms, Chl, Vrm	0.24	0.26	$2M_1$–$3T$	9.0252	n.d.
MG-63	Gray schist	Qz, Kfs, Hem, Ms, Chl, (C/V)	0.26	0.25	$2M_1$	9.0228	
MG-64	Black schist	Qz, Kfs, Hem, Ms, Chl, (C/V)	0.23	0.23	$2M_1$–$3T$	9.0204	9.0546
MG-65	Smoke blue schist	Qz, Kfs, Hem, Ms, Chl	0.23	0.23	$2M_1$–$3T$	9.0204	9.0546

3. Methods

3.1. X-Ray Diffraction (XRD)

Samples were washed and, after coarse crushing, homogeneous rock chips were used for preparation of samples for XRD. XRD analyses were carried out using a Philips X'Pert PRO MPD powder diffractometer (University of Málaga, Málaga, Spain) with CuKα_1 radiation, voltage of 45kV and a current of 35 mA, Ge monochromator, and automatic divergence slit. Two size fractions (2–20 μm and <2 μm) were separated by centrifugation through a column of water, on the basis of Stokes's law. Oriented aggregates were prepared by sedimentation on glass slides. Ethylene glycol (EG) and heat treatments were carried out to corroborate the identification of smectite, vermiculite, mixed-layer illite/smectite, and mixed-layer chlorite/vermiculite on the basis of the expandability of these phases. Preparation of samples and experimental conditions for measurements of illite "crystallinity" (Kübler Index, KI) of the <2 μm fraction were carried out according to IGCP 294 IC Working Group recommendations [43]. The KI measurements (x) were transformed into crystallinity index standard (CIS) values (y) according to the equation, y = 1.9794x − 0.0733, obtained in the laboratory using the international standards of Warr and Rice [44]. The *b* parameter of mica was obtained from the (060) peak measured on the whole-rock powdered samples [45]. For all the measurements of spacings, quartz from the sample itself was used as an internal standard. In this contribution, a simple qualitative estimate of the existence of mica polytypes based on the presence of the 1*M* 112 and $11\bar{2}$, $2M_1$ $11\bar{4}$ and 3*T* $10\bar{1}5$, $10\bar{1}7$, and $10\bar{1}8$ reflections were also done according to Bailey [46].

3.2. X-Ray Fluorescence (XRF)

Whole-rock analyses of the major elements of selected samples were carried out using X-ray fluorescence in a Philips Magix Pro (PW-2440) spectrometer (Centro de Instrumentación Científica, CIC, University of Granada, Granada, Spain). Glass beads with lithium tetraborate were employed to minimize the preferential orientation of phyllosilicates. The detection limit for major elements was 0.01 wt.%. Loss on ignition (LOI) was determined using 0.5 g of powdered sample, first dried at 110 °C and then heated at 1000 °C for one hour. The proportion of ferrous iron was determined by wet-chemical analyses, specifically, by the volumetric method. Crushed and dried samples were decomposed by a mixture of H_2SO_4 (98%) and HF (48%) in a graphite crucible with a cover of Ni at reducing atmosphere. The released Fe^{2+} was titrated with $K_2Cr_2O_7$ 1/20 N solution in the presence of H_3PO_4, using 10 drops of 0.2% sodium diphenylamine sulphonate as the redox indicator (modified after Pratt's method [47]).

3.3. Electron Microscopy

Following the XRD and optical studies, polished and carbon-coated thin sections were prepared for imaging using back-scattered electrons (BSEs) with a scanning electron microscopy (SEM) to obtain textural and chemical data. These observations were carried out using two microscopes both in the CIC (University of Granada, Granada, Spain): (a) A ZEISS DSM 950 scanning electron microscope equipped with an X-ray energy-dispersive (EDX) system (LINK QX 2000) at an accelerating voltage of 14 kV and 2 nA beam current; and (b) a LEO 1430VP with a EDX system, at an accelerating voltage of 20 kV, 1 nA beam current, and counting time of 100 s per step to analyze the phyllosilicates using both natural and synthetic standards: albite (Na), orthoclase (K), periclase (Mg), wollastonite (Si, Ca), and synthetic Al_2O_3 (Al), Fe_2O_3 (Fe) and $MnTiO_3$ (Ti and Mn). Analytical data were ZAF (atominc number, absorption and fluorescence) corrected.

Due to the very fine-grained nature of some of the studied clastic rocks, a high-resolution transmission electron microscopy (HRTEM) study was carried out on ion-milled and carbon-coated Cu-rings preparations. Three different microscopes were used: (a) A Philips CM20 scanning transmission electron microscope (STEM) operating at 200 kV, with LaB_6 filament and a point-to-point

resolution of 2.7Å in the TEM mode and 50 Å in the STEM mode (CIC, University of Granada, Granada, Spain); (b) a JEOL JEM 2100 STEM operating at 200 kV and with a point-to-point resolution of 2.5 Å in the TEM mode (National Electron Microscopy Center, Complutense University of Madrid, Madrid, Spain); and (c) a JEOL JEM 300F STEM operating at 300 kV and with a point-to-point resolution of 1.7 Å in the TEM mode (National Electron Microscopy Center, Complutense University of Madrid, Madrid, Spain). Lattice-fringe images of phyllosilicates were obtained using (001) reflections. The EDX spectra of ion-milled samples performed on the Philips CM20 were obtained using a raster of (0.10 × 0.02) μm in scanning mode to minimize alkali diffusion and volatilization with the long axis oriented parallel to the length of phyllosilicate packets. Counting times were 100 s except for Na and K, which were analyzed using counting times of 30 s to minimize alkali-loss problems as short counting times improve reproducibility for K and Na [48]. The analytical electron microscopy (AEM) quantitative chemical analyses were calculated from the EDX spectra using standards (albite, olivine, biotite, spessartine, muscovite, chlorite, and titanite) to obtain k-factors for transformation of intensity ratios to concentration ratios according to the approximation of Cliff and Lorimer [49]. The structural formulae of micas (illite-muscovite, paragonite, and intermediate Na-K and Na-Ca micas) and pyrophyllite were calculated on the basis of 22 negative charges $O_{10}(OH)_2$. The chlorite, chlorite-rich mixed-layer compositions, and kaolinite were calculated on the basis of 28 negative charges $O_{10}(OH)_8$.

3.4. Thermometric Methods

Semi-empirical thermometric methods [15,16] were applied in chlorites analyzed by SEM under the conditions previously indicated. The choice of these two chlorite thermometers was guided by the compositional range of the studied chlorites, and by the *T* range. In both cases, the structural site location of Ti, Mn, Na, Ca, and K was done considering the configuration followed by each author. In addition, all iron was considered as Fe^{2+}.

The uncertainties on the temperatures calculations are approximately ±50 °C [16].

4. Results

4.1. Petrography

The XRD analysis and petrographical and electron microscopy studies showed that quartz, feldspars and K-micas are the principal phases in all samples (Tables 1 and 2). Specifically, the phyllosilicates present in the Ghomaride complex are illite, kaolinite, and minor quantities of mixed-layer illite/smectite and chlorite in the Beni Hozmar unit. Koudiat Tiziane unit is mainly characterized by illite and some kaolin group minerals (kaolinite and/or dickite) with a minor presence of trioctahedral chlorite and sudoite, and the deepest unit, Aakaili, shows illite, dickite, sudoite, and Na-K intermediate mica. In addition, samples from the intermediate unit (Koudiat Tiziane) have carbonates (dolomite or calcite) and Fe-oxides are present in the reddish samples. With respect to the Federico unit samples, the phyllosilicates characteristics of the Tizgarine unit are illite, pyrophyllite and minor dickite, Na-K intermediate mica, trioctahedral chlorite, and sudoite. Boquete Anjera and Beni Mezala units also show paragonite and intermediate white micas. Occasionally, in the deepest samples (Beni Mezala), talc, vermiculite, and mixed layer chlorite/vermiculite were detected.

4.1.1. Sandstones

Specifically, sampled sandstones, which appear distributed along the whole sequence, show a moderate diversity and are mainly quartzarenites (>95% quartz), sublitharenites, and subarkoses, although sandstones from the deepest Federico units (Boquete Anjera and Beni Mezala) are orthoquartzites. In general, the ghomaride and tizgarine sandstones show a framework formed by quartz grains, which range from tens to several hundred of μm in diameter with varied shapes. The detrital minerals in these units are quartz, feldspars (sanidine and oligoclase), lithic fragments (sedimentary and metamorphic), and phyllosilicate flakes (di- and trioctahedral micas and chlorite).

Detrital phyllosilicates were identified based on their large size, homogeneity of individual grains, and, in general, well-crystallized aspect (Figure 4a). The matrix is scarce and mostly composed of quartz and very fine-grained hematite. The presence of Fe-oxides in the matrix is responsible for the reddish color of the ghomaride sandstones in hand samples. The cement, which completely fills the porosity, is clayey, mainly kaolinitic in the Beni Hozmar and Koudiat Tiziane samples and with the appearance of dickite, illite, and sudoite in the deepest ghomaride samples (Figure 4b). The cement in the sandstones of the Tizgarine unit consists of fine-grained dickite with a variable degree of transformation into white mica, sudoite, and pyrophyllite. The whitish orthoquartzites present in the deepest Federico units are characterized by a framework of smaller quartz grains, with phyllosilicate intercalations (white mica and, sometimes, chlorite) showing a cleavage development more evident in the Beni Mezala sandstones (Figure 4c).

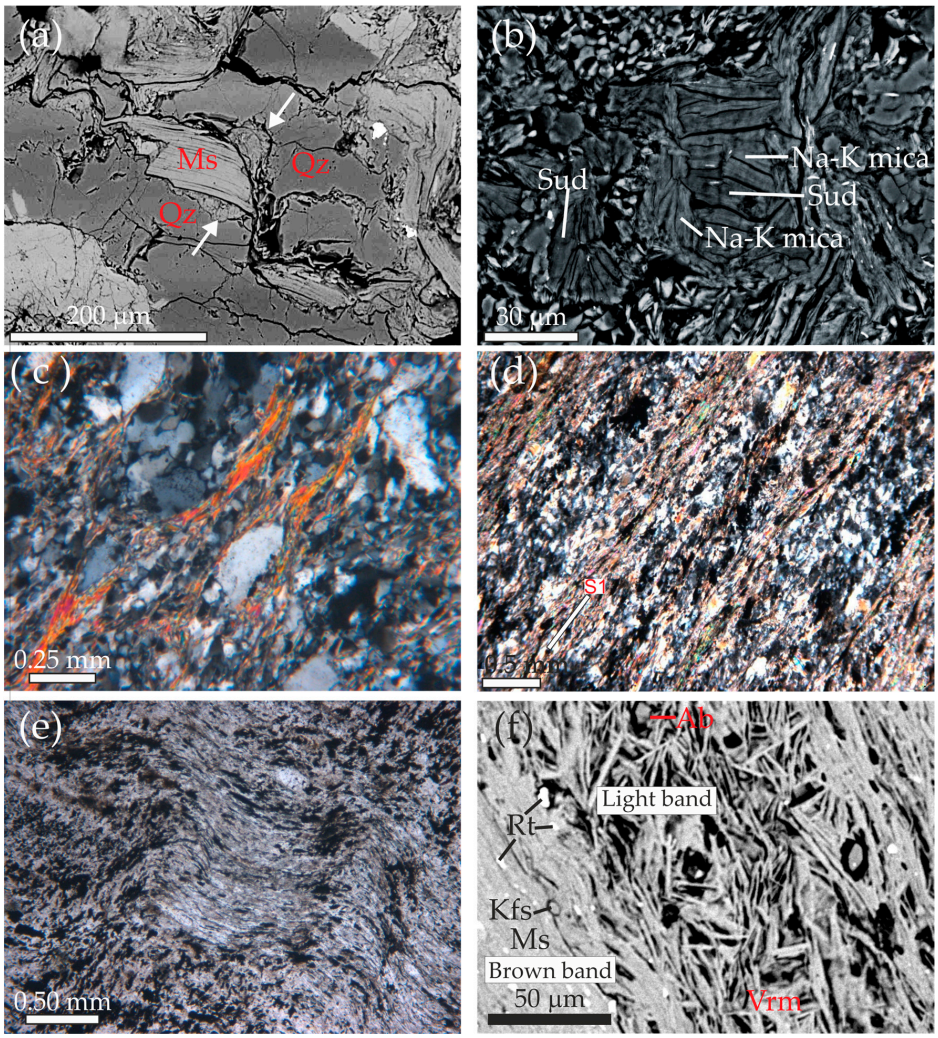

Figure 4. Microscopy images showing the aspect of the sandstones and metapelites: (**a**) backscattered electron (BSE) image corresponding to a ghomaride sandstone with a detrital white mica surrounded by quartz grains and pore-filling cement (white arrows); (**b**) BSE image of the pore-filling cement mainly composed of sudoite and Na-K mica; (**c**) Beni Mezala sandstone (Federico units) with alternation of quartz and phyllosilicate bands showing an incipient cleavage development (petrographical image with crossed nicols); (**d**) Beni Mezala phyllite with a well-developed foliation (petrographical image, crossed nicols); (**e**) Beni Mezala phyllite with an incipient crenulation (petrographic image, crossed nicols); (**f**) BSE image corresponding to a detail of the light and brown bands (under petrographic microscope) from Beni Mezala whitish schist; for further explanation see the text.

4.1.2. Phyllites and Schists

Phyllites and schists are the predominant lithologies in Boquete Anjera and Beni Mezala units (Table 2). Finely grained phyllites display a well-developed slaty cleavage defined by parallel, preferentially oriented packets of phyllosilicates (K and Na dioctahedral micas and trioctahedral chlorite, Figure 4d), and elongated quartz grains as well as feldspars, rutile, and hematite. Locally, the main cleavage is affected by an incipient crenulation (Figure 4e). The whitish schist described in Beni Mezala unit is composed of light and brown alternating sub-parallel millimeter bands. The lightest ones are characterized by disoriented very fine-grained phyllosilicates (white mica, vermiculite, and kaolin group minerals), quartz, and albite. However, the brown bands show a well-developed cleavage defined by K-dioctahedral micas with many inclusions of rutile, vermiculite, and K-feldspar (Figure 4f). Interstratified chlorite/vermiculite was detected in the darkest bands. Nevertheless, talc was not recognized by imaging (neither optic nor BSE) although it was detected by XRD in the whitish schist (Table 2). Probably, the talc is interstratified with other phyllosilicates at the nanometer scale.

4.2. Crystal-Chemical Parameters

The CIS values for both sandstones and metapelites reveal an increase in metamorphic grade from typical diagenetic-low grade anchizone values (1.50–0.37 $\Delta°2\theta$, Table 1) in the Ghomaride complex to upper anchizone (Tizgarine)-epizone (Boquete Anjera and Beni Mezala) conditions (0.43–0.21 $\Delta°2\theta$, Table 2) in the Federico units according to the revised anchizone boundaries of the CIS scale (from 0.52 to 0.32 $\Delta°2\theta$) [50]. The significant variation in values for different samples in the Ghomaride complex is typical of the diagenesis [51]. In addition, most of the Ghomaride complex samples have CIS values larger than those of the EG-treated samples (Figure 5), probably implying the presence of smectite layers interstratified with diagenetic illite.

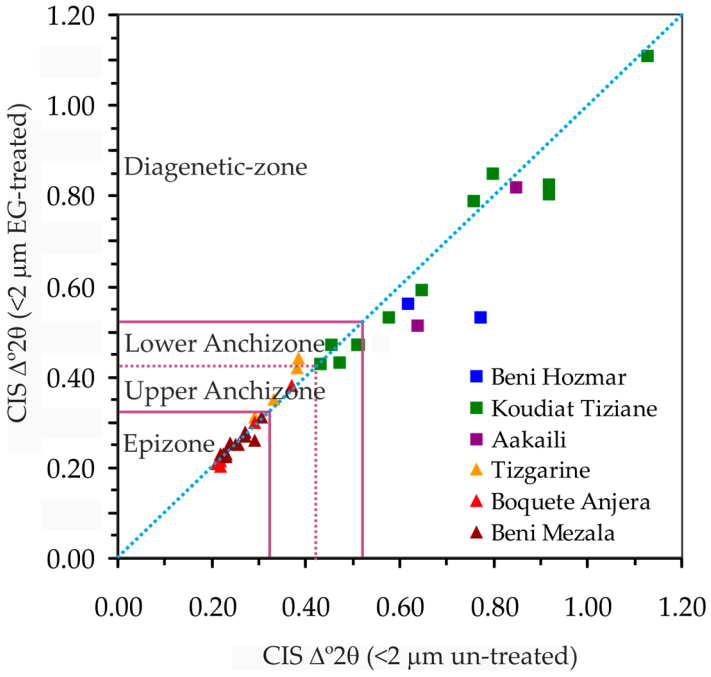

Figure 5. Diagram of CIS values from the <2 μm untreated vs. <2 μm EG-treated samples.

The illite-muscovite polytypes analysis shows the presence of the $2M_1$ in all the studied samples coexisting with the $1M$ in some of the ghomaride samples (Table 1) and with the $3T$ in some of the Federico units (Table 2).

An average of 9.004 Å (σ = 0.008) was obtained for the *b* cell parameter of dioctahedral micas in the ghomaride samples (Table 1), whereas the average for the Federico units was 9.010 Å (σ = 0.012). If

considering only samples where $2M_1$ polytype and $3T$ polytype (indicative of high-pressure conditions, H*P*; [52–54]) coexist (Figure 6), the average *b* parameter increases softly up 9.017 Å (σ = 0.006). Nevertheless, the average corresponding to the Federico samples with only the $2M_1$ polytype is 9.005 Å (σ = 0.013).

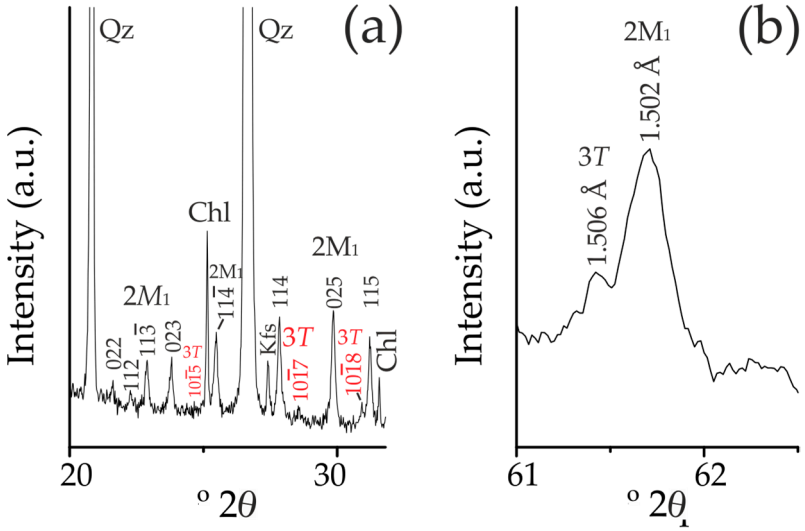

Figure 6. Selected zones of the XRD pattern of the deepest Federico unit samples: (**a**) positions of the *hkl* peaks of $2M_1$ and $3T$ polytypes of dioctahedral white micas; (**b**) position of the 060 peaks of two dioctahedral white micas (enlarged and smoothed profile).

4.3. Chemical Bulk Composition

Chemical analyses of the major elements of sandstones and metapelites are given in Table 3. The comparison of these data with the reference average of Post-Archean Australian Shales (PAAS), published by Taylor and McLennan [55] shows that the sandstones are richer in Si and poorer in Al and Fe than the PAAS and coeval metapelites. The metapelites show average contents very similar to the PAAS, although Na and Ca are slightly lower and K values a bit higher than in PAAS.

4.4. TEM Observations

Based on XRD and petrographic data, six samples corresponding to different units of the studied sequence were chosen for HRTEM study specially focused on the phyllosilicates: MG-44 (Koudiat Tiziane, Ghomaride), MG-56 (Aakaili, Ghomaride), MG-21 (Boquete Anjera, Federico), MG-62 (Beni Mezala 2, Federico), and the deepest ones, MG-18 and MG-14 (Beni Mezala 1, Federico). The HRTEM characterization confirms the general mineralogical data determined by XRD and SEM for the different units of the studied area but also allowed deepening in the very fine-grained phyllosilicates identification or in the textural relations among phyllosilicates and their chemistry at the nanometer scale.

Deep diagenetic lutite MG-44 is mainly composed of illite and chlorite. The low-magnification images show illite packets with both parallel and contact-angle boundaries. The thickness of the packets ranges between tens and a few hundreds of amstrongs, typical of diagenetic clays. $2M_1$ and $1M$ polytypes were identified on the basis of selected area electron diffraction patterns (SAED); this observation is in accord with the periodicities of the lattice fringes, showing 10 Å and 20 Å periodicities (Figure 7a). In some cases, lattice fringe images reveal contrast differences, suggesting the presence of smectite interlayers (light contrast, Figure 7b), which is in coherence with the observations made in Figure 5 with respect to the variations in the CIS values between the <2 μm vs. <2 μm EG-treated fractions. In addition, AEM analyses of these areas have relatively high Si and low K contents, confirming the mixed layering.

Table 3. Whole-rock analyses of major elements (oxide wt.%) of ghomaride and federico samples.

Unit		Sample	SiO_2	Al_2O_3	Fe_2O_3	FeO	MnO	MgO	CaO	Na_2O	K_2O	TiO_2	P_2O_5	LOI	Total	(1) Al_2O_3	(1) Fe_2O_3	(1) FM	(1) CaO	(1) KNa
Ghomaride complex	Koudiat Tiziane	MG-44	62.11	19.42	7.33	n.d.	0.02	1.64	0.08	<LLD	5.79	0.89	0.13	2.11	99.52	56.65	21.38	4.84	0.23	16.89
		MG-46	67.34	11.79	3.74	0.49	0.07	2.74	2.52	0.14	3.25	0.71	0.08	6.40	99.27	47.66	15.12	3.59	10.19	13.70
		MG-47	58.84	10.99	2.44	0.94	0.27	5.14	6.45	0.45	2.53	0.64	0.11	11.89	100.69	37.62	8.35	21.74	22.08	10.20
		MG-48	67.00	17.05	5.28	0.73	0.03	1.13	0.10	0.57	2.82	0.96	0.04	4.03	99.73	61.53	19.05	6.82	0.36	12.23
		MG-49	69.90	14.62	4.36	1.26	0.04	1.23	0.17	0.88	2.23	0.85	0.07	3.36	98.97	58.98	17.59	10.21	0.69	12.55
		MG-50	69.06	14.97	4.54	0.98	0.03	1.35	0.28	0.83	2.36	0.88	0.07	3.72	99.08	59.08	17.92	9.31	1.10	12.59
	Aakaili	MG-57	57.36	21.73	7.50	1.22	0.04	1.24	0.02	0.24	4.65	1.02	0.07	4.70	99.79	59.31	20.47	6.82	0.05	13.35
Federico units	Tizgarine	MG-37	69.56	16.83	5.60	0.77	0.01	0.30	0.09	<LLD	2.86	0.97	0.13	2.65	99.76	63.61	21.16	4.08	0.34	10.81
		MG-35	53.39	11.40	22.18	2.97	0.45	0.85	0.10	0.00	1.69	0.58	0.12	5.20	98.93	28.76	55.95	10.77	1.48	4.26
		MG-34	85.79	9.64	0.24	0.31	0.01	0.08	0.05	<LLD	0.37	0.61	0.04	1.96	99.11	90.09	2.24	3.74	0.47	3.46
	Boquete Anjera	MG-23f	40.86	32.26	10.32	n.d.	0.05	2.62	0.79	1.59	5.00	1.48	0.17	4.32	99.46	61.30	19.61	5.07	1.50	12.52
		MG-22	44.66	28.75	7.50	1.88	0.08	3.70	0.59	1.13	4.04	1.25	0.31	5.54	99.43	60.31	15.73	11.87	1.24	10.85
		MG-21	54.68	23.01	6.82	1.61	0.03	2.88	0.23	0.64	4.87	1.02	0.11	3.66	99.55	57.40	17.01	11.27	0.57	13.74
		MG-11	69.13	15.77	5.18	0.49	0.04	1.58	0.07	<LLD	4.39	0.79	0.06	2.20	99.69	57.30	18.82	7.67	0.25	15.95
		MG-11′	88.82	5.70	0.21	0.84	0.04	0.50	0.07	<LLD	1.61	0.35	0.04	1.09	99.27	63.55	2.34	15.38	0.78	17.95
		MG-7	79.86	10.46	0.47	1.43	0.01	0.75	0.03	<LLD	3.67	0.44	0.03	2.97	100.12	62.19	2.79	13.02	0.18	21.82
		MG-9	59.83	19.76	6.58	0.49	0.03	3.04	0.04	0.10	5.20	0.89	0.04	3.64	99.64	56.07	18.67	10.13	0.11	15.04
		MG-10	68.91	13.31	4.05	0.56	0.02	1.54	0.04	<LLD	4.03	0.77	0.04	7.29	100.56	56.52	17.20	9.00	0.17	17.11
	Beni Mezala 2	MG-62	57.30	20.97	6.87	0.98	0.01	2.01	0.02	0.04	6.24	0.96	0.07	3.56	99.03	56.46	18.50	8.08	0.05	16.91
	Beni Mezala 1	MG-19	93.95	2.61	0.13	0.35	0.01	0.14	0.02	<LLD	0.81	0.37	0.03	0.58	99.00	64.13	3.19	12.29	0.49	19.90
		MG-18	54.30	21.89	3.79	1.75	0.05	4.54	0.07	0.04	5.77	0.81	0.12	6.33	99.46	57.76	10.00	16.73	0.18	15.33
		MG-18′	87.47	6.06	0.00	1.40	0.01	0.89	0.03	0.00	1.54	0.64	0.03	1.65	99.72	61.03	0.00	23.16	0.30	15.51
		MG-15	59.77	21.24	7.39	0.35	0.06	1.01	0.41	1.20	3.93	1.05	0.19	3.24	99.84	59.68	20.76	3.99	1.15	14.41
		MG-14	55.25	20.97	4.52	3.76	0.01	2.01	1.02	1.04	6.24	0.96	0.07	3.56	99.41	52.99	11.42	14.61	2.58	18.40
		MG-13	60.75	20.11	5.59	1.68	0.04	1.83	1.14	1.14	3.29	0.95	0.11	3.48	100.11	57.75	16.05	10.20	3.27	12.72
		RMG13 Df	50.48	23.31	5.00	2.52	0.15	1.22	7.39	1.03	3.34	1.02	0.10	3.62	99.18	53.03	11.37	8.85	16.81	9.94
		RMG13 Af	50.40	26.85	8.59	1.53	0.03	1.21	1.00	1.35	3.82	1.30	0.26	3.40	99.74	60.50	19.36	6.24	2.25	11.65
		MG-64	55.25	22.93	6.20	1.95	0.01	1.37	0.14	0.01	7.24	0.90	0.14	3.39	99.53	57.54	15.56	8.36	0.35	18.19
		MG-65	64.73	17.75	4.08	1.61	0.01	1.13	0.13	<LLD	5.56	0.86	0.10	3.65	99.61	58.64	13.48	9.08	0.43	18.37
		PAAS	62.80	18.90		6.50	0.11	2.20	1.30	1.20	3.70	1.00	0.16	6.00	99.90	55.74	0.00	25.98	3.83	14.45

(1) Normalized content of Al_2O_3, Fe_2O_3, FM, CaO and KNa (oxide wt.%), where FM = FeO + MgO + MnO and KNa = K_2O + Na_2O. n.d.: not determined; <LLD: Lower Limit Detection. LOI: Loss On Ignition.

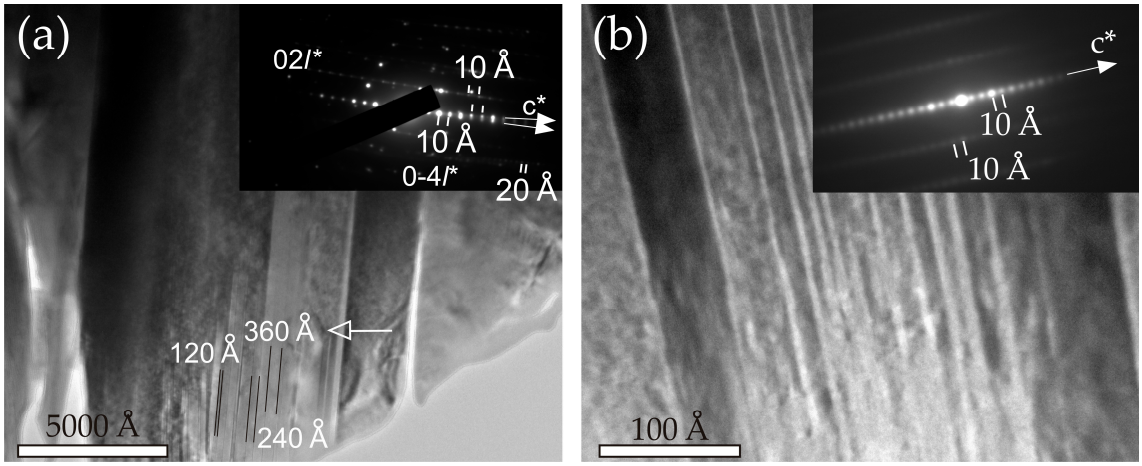

Figure 7. TEM images corresponding to diagenetic lutite MG-44 (Ghomaride): (**a**) illite packets with well-defined boundaries; 1*M* and $2M_1$ polytypes are present in the SAED (see inset); (**b**) low-magnification image of illite packets with contrast differences implying the presence of smectite-like (light fringes) layers. SAED pattern shows 10 Å periodicity.

Sandstone MG-56 is characterized by a cement with a greater phyllosilicate diversity (illite, Na-K mica, dickite and sudoite). According to Ruiz-Cruz et al. [3], this is a lower anchizone sample in spite of its deep diagenetic CIS value probably due to the presence of Na-bearing mica. TEM images reveal the presence of all these phyllosilicates showing parallel boundaries and with one included within the other and even forming mixed layers (Figure 8).

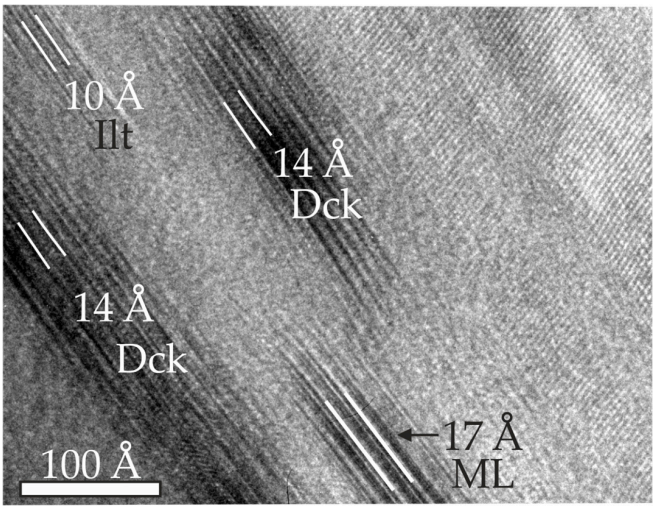

Figure 8. Lattice-fringe image showing the coexistence of illite, dickite, and mixed layers (ML) at the nanometer scale (sandstone MG-56, Ghomaride; modified from Ruiz Cruz et al. [3]).

In relation to the Federico units' samples, epizonal metapelite MG-21 includes muscovite, Na-K intermediate mica, and a minor presence of paragonite and chlorite. The most evident features of this sample at the nanometer scale is the thickness of the phyllosilicate packets, in most of the images >500 Å, and the variety of orientations from parallel to well-defined high-angle grain boundaries (Figure 9a). Grain sizes of dioctahedral micas with different interlaminar composition are approximately equal (Figure 9b), suggesting their formation under the same conditions. In addition to the presence of Na-K micas, muscovite and paragonite, both $2M_1$, coexist as separate crystals (Figure 9c). Chlorite packets are clinochlore (Mg/(Mg + Fe) = 0.84), with a few thousands of amstrongs thick and SAED patterns with sharp reflections consistent with large, defect-free crystals (Figure 9d).

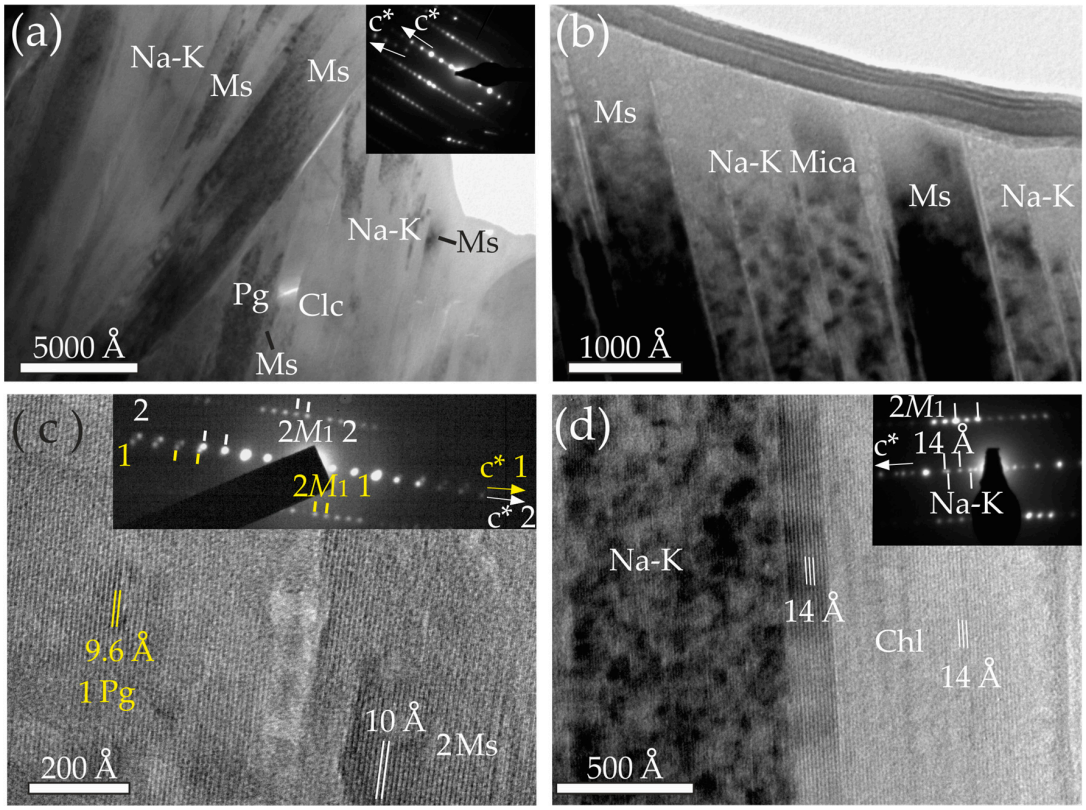

Figure 9. TEM images corresponding to a phyllite (MG-21, Federico units): (**a**) textural relation among phyllosilicates (muscovite, Na-K mica, paragonite and trioctahedral chlorite); (**b**) lattice-fringe image showing the relation between K-dioctahedral micas and Na-K dioctahedral micas; and (**c**) lattice-fringe image showing the coexistence of paragonite and muscovite. Identifications were based in part on AEM analyses. The inset SAED pattern shows well-defined reflections indicating for both phases a two layers polytype; (**d**) thick packets of chlorite and mottled Na-K mica with net parallel boundaries.

Sample MG-62 is an epizonal metapelite, with a slaty cleavage defined by parallel, preferentially oriented packets of phyllosilicates, mainly large crystals of muscovite and trioctahedral chlorite (>3000 Å).

The study of the whitish schist MG-18 at the TEM scale has focused on the Mg-rich areas, the dark bands described previously and which are characterized by a slaty cleavage defined mainly by K-dioctahedral micas but also by vermiculite and K-feldspar (Figure 4f). In low-magnification images, chlorite/vermiculite mixed-layers (C/V) developing lenticular voids are observed, probably as a consequence of the vacuum collapse (Figure 10a). The identification of C/V is based also on the SAED patterns and on the presence of packets with 24 Å layers in the lattice fringe images (Figure 10b). In addition, TEM images reveal that both $2M_1$ muscovite and vermiculite occur as large, defect-free crystals, more than 1000 Å thick (Figure 10c).

Sample MG-14, an epizonal metapelite with a well-developed slaty cleavage, contains a varied presence of phyllosilicates: muscovite, Na-K mica, Na-Ca mica, paragonite, chlorite, and subordinate pyrophyllite. The phyllosilicates are mostly defect-free crystals with more than several 1000 Å thick coexisting dioctahedral micas with different interlaminar composition as separate crystals (Figure 11a). AEM data reveal the presence of Na-K mica with an average of $Ms_{60}Pg_{40}$, whose projection falls close to one limb of the solvus between the muscovite and paragonite system. Chlorite packets, crystalline in appearance and uniform, with a few thousands of amstrongs thick and an ordered polytype (Figure 11b), are clinochlore (Mg/(Mg + Fe) = 0.77). Occasionally, periodicities of 20 Å were detected in 14 Å areas (Figure 11c).

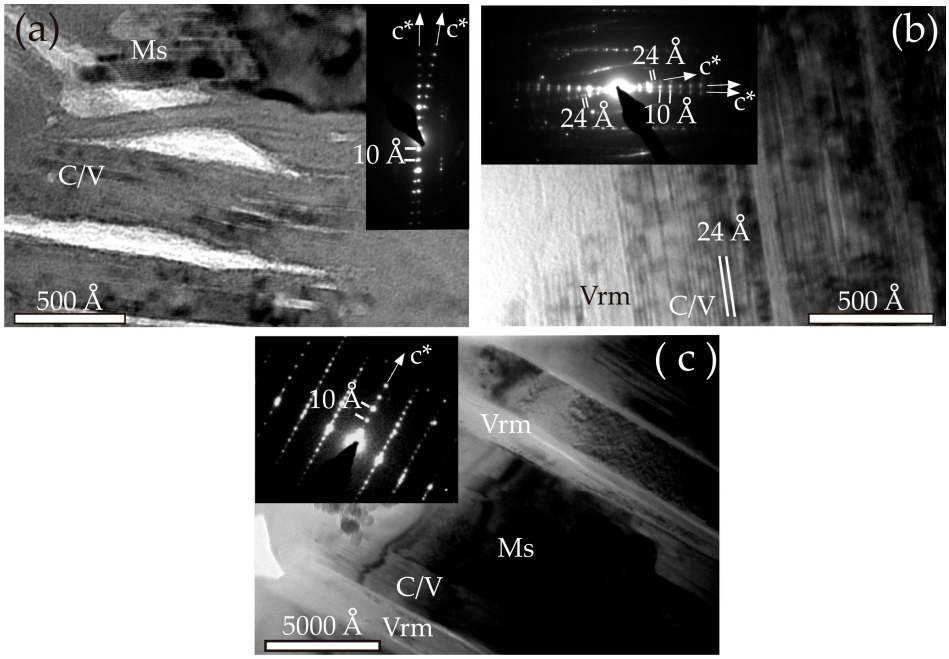

Figure 10. Nanometer scale view of the "dark" bands distinguished by petrographic microscopy in the MG-18 schist (Federico units): (**a**) phyllosilicate packets (10 Å periodicity, see SAED) with lenticular voids; (**b**) lattice-fringe image and SAED showing 24 Å periodicity, which corresponds to chlorite/vermiculite mixed-layers; and (**c**) thick crystals of muscovite and vermiculite (>1000 Å). C/V: mixed-layers chlorite/vermiculite.

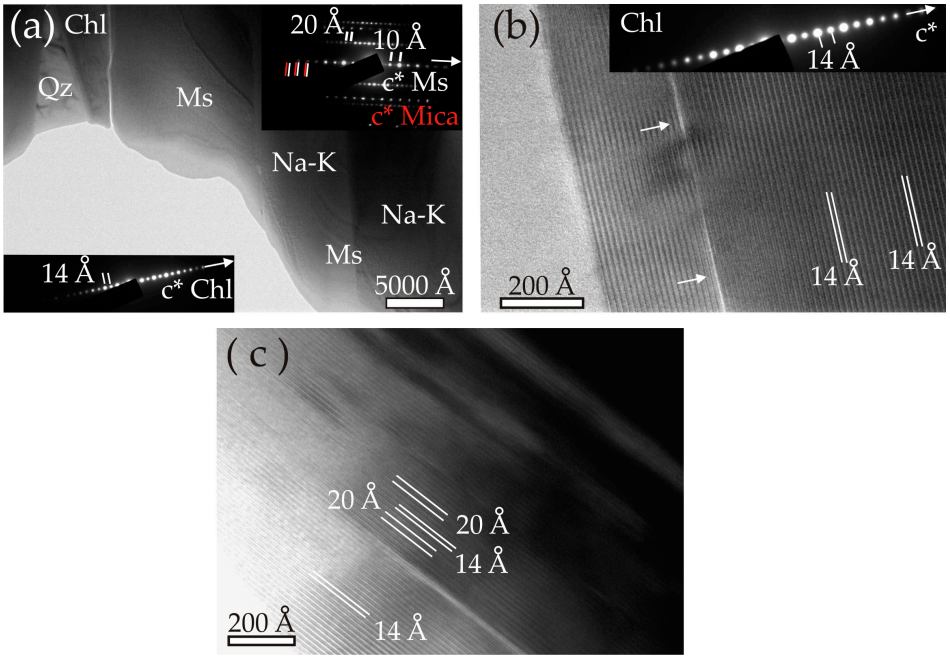

Figure 11. TEM images showing defect-free crystals corresponding to the phyllite MG-14 (Federico units): (**a**) several dioctahedral mica packets with different interlayer contents; (**b**) chlorite packets with clinochlore composition; and (**c**) 20 Å periodicities (Ms) inside 14 Å packets (Chl).

4.5. Chemical Composition of Phyllosilicates

The chemical compositions of the phyllosilicates were determined mostly by EDX on the SEM except for some cases in which the EDX spectra of ion-milled samples studied in the TEM have helped

the chemical characterization of very fine-grained phyllosilicates under the conditions previously indicated in the methods section.

4.5.1. Dioctahedral Micas

The average structural formulae of K-rich dioctahedral micas of authigenic origin, corresponding to samples from different units, are presented in Table 4. Authigenic micas corresponding to the ghomaride sandstones display deficiencies in interlayer cations, with this observation being consistent with the presence of illite/smectite mixed layers described above (Figures 5 and 7b) and the excess of Si, mainly caused by both illitic (Figure 12a) and phengitic components (Figure 12b). In addition, Na contents are significant in some of the analyzed illites (up to 0.32 *apfu* in the Aakaili analyses). In the Federico units, K-dioctahedral micas corresponding to the Tizgarine unit (MG-34) are more homogeneous but also with a clear illitic substitution (Figure 13). Nevertheless, Boquete Anjera and Beni Mezala analyses, in spite of the heterogeneity, are close to true muscovite, with interlayer cation sums close to 1 *apfu* in most cases (Figure 13a). This is in accord with the epizonal grade of these samples, where, according to Abad et al. [56], the illitic component becomes insignificant. In any case, in micas from Federico units, the proportions of Si, Al, and Fe + Mg are mostly controlled by the phengitic and the ferrimuscovitic vectors (Figure 13b). However, the white micas with the highest Si and Fe + Mg contents show high Mg values and deficits in the interlaminar content (white micas in the whitish schist); this trend could represent contamination by trioctahedral phases (Figure 10a,c).

Typical compositions of micas intermediate to the end-members muscovite-paragonite and paragonite-margarite, called Na-K and Na-Ca micas respectively, were also analyzed in samples from the Federico units (Table 5). These compositions are quite variable, expanding the entire range from muscovite to paragonite in the case of the Na-K micas (Figure 14).

The analyses of detrital-like micas of an anchizonal sandstone of the Ghomaride complex and epizonal quartzites from the Beni Mezala units (Table 6) were compared with the data of the authigenic ones from the same samples (Figure 15). These data show that the detrital micas are more heterogeneous than authigenic micas, suggesting potential different sources for the different studied units. In addition, whereas detrital mica and chlorite coexist with authigenic phases in the uppermost slices, at increasing tectonic depths, micas and chlorite with detrital signals are almost lacking.

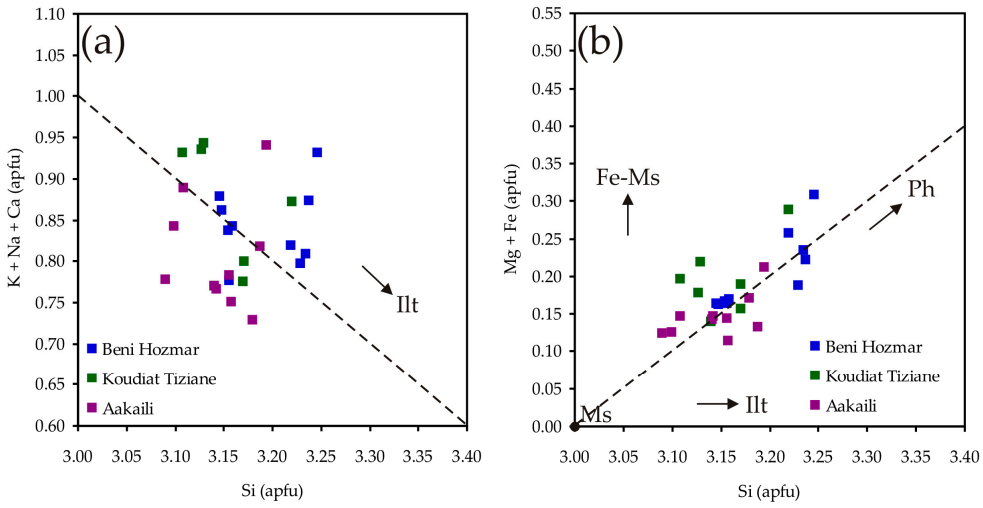

Figure 12. Relationships among chemical components of authigenic dioctahedral micas from the Ghomaride Complex: (**a**) Si vs. K + Na + Ca, the dotted line corresponds to the ideal illitic substitution (Ilt); (**b**) Si vs. Mg + Fe, the dotted line corresponds to the ideal phengitic substitution (Ph). Fe-Ms: the ferri-muscovitic exchange vector. Solid circles indicate values for the theoretical muscovite (Ms).

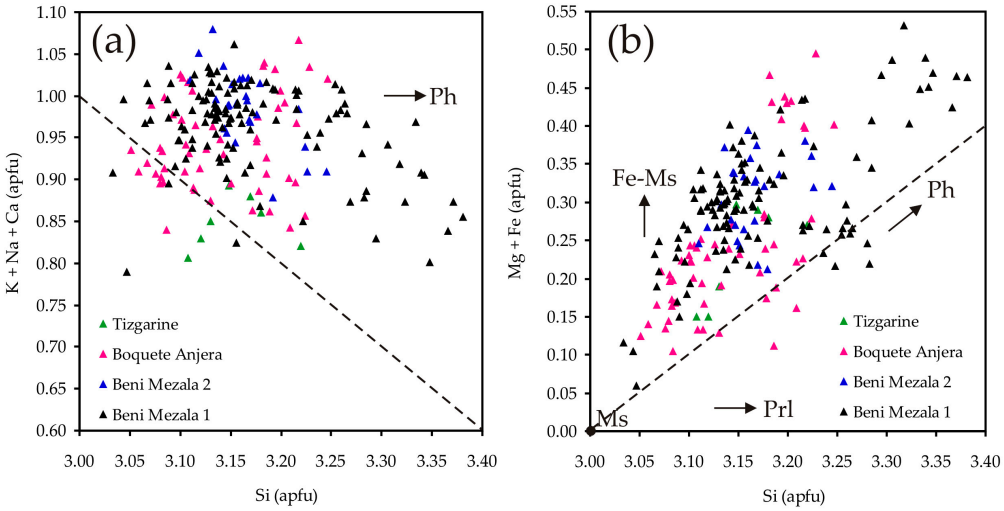

Figure 13. Relationships among chemical components of authigenic dioctahedral micas from the Federico units: (**a**) Si vs. K + Na + Ca, the dotted line corresponds to the ideal illitic substitution; (**b**) Si vs. Fe + Mg, the dotted line corresponds to the ideal phengitic substitution (Ph). Fe-Ms: the ferri-muscoviti exchange vector; Prl: Pyrophyllitic exchange vector. Solid circles indicate values for the theoretical muscovite (Ms).

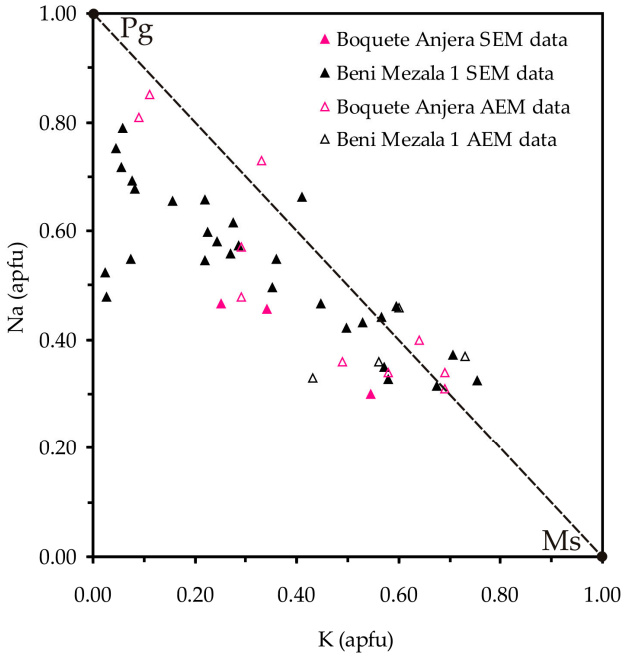

Figure 14. Compositional diagram showing the K and Na contents of intermediate white micas from the Federico units. Solid circles indicate values for the theoretical muscovite (Ms) and paragonite (Pg).

Table 4. Average structural formulae for authigenic white micas from Ghomaride and Federico units obtained by SEM/EDX and normalized to $O_{10}(OH)_2$.

Unit/Sample		Si	^{IV}Al	^{VI}Al	Ti	Fe^{2+}	Mg	Ca	K	Na	Σ Oct.	Σ Inter.	Al^t	#Mg
Ghomaride complex														
Beni Hozmar														
BH-3	Mean	3.19	0.81	1.84	0.01	0.08	0.13	0.02	0.77	0.05	2.05	0.84	2.64	63
n = 10	*SD*	*0.04*	*0.04*	*0.05*	*0.01*	*0.03*	*0.03*	*0.03*	*0.04*	*0.01*	*0.02*	*0.05*	*0.09*	*7*
Koudiat Tiziane														
MG-40	Mean	3.18	0.82	1.85	0.01	0.08	0.13	0.00	0.70	0.12	2.07	0.81	2.67	63
n = 3	*SD*	*0.04*	*0.04*	*0.09*	*0.00*	*0.03*	*0.04*	*0.00*	*0.13*	*0.07*	*0.01*	*0.05*	*0.13*	*2*
MG-49	Mean	3.13	0.87	1.85	0.01	0.08	0.11	0.01	0.86	0.03	2.05	0.90	2.71	57
n = 4	*SD*	*0.03*	*0.03*	*0.04*	*0.01*	*0.03*	*0.00*	*0.01*	*0.07*	*0.03*	*0.01*	*0.08*	*0.03*	*8*
Aakaili														
MG-56	Mean	3.15	0.85	1.91	0.00	0.06	0.08	0.01	0.59	0.21	2.06	0.81	2.77	55
n = 10	*SD*	*0.04*	*0.04*	*0.05*	*0.00*	*0.01*	*0.02*	*0.02*	*0.11*	*0.06*	*0.02*	*0.07*	*0.07*	*8*
Federico units														
Tizgarine														
MG-34	Mean	3.15	0.85	1.82	0.03	0.14	0.10	0.00	0.78	0.07	2.08	0.85	2.67	40
n = 7	*SD*	*0.04*	*0.04*	*0.05*	*0.01*	*0.03*	*0.04*	*0.00*	*0.05*	*0.02*	*0.02*	*0.03*	*0.08*	*6*
Boquete Anjera														
MG-23f	Mean	3.13	0.87	1.86	0.01	0.12	0.06	0.02	0.75	0.13	2.06	0.90	2.73	33
n = 15	*SD*	*0.05*	*0.05*	*0.03*	*0.01*	*0.03*	*0.01*	*0.01*	*0.05*	*0.03*	*0.03*	*0.04*	*0.08*	*6*
MG-23	Mean	3.10	0.90	1.87	0.01	0.11	0.06	0.00	0.77	0.13	2.06	0.90	2.77	33
n = 11	*SD*	*0.04*	*0.04*	*0.04*	*0.01*	*0.02*	*0.03*	*0.00*	*0.04*	*0.04*	*0.02*	*0.02*	*0.07*	*10*
MG-21	Mean	3.17	0.83	1.81	0.02	0.12	0.11	0.00	0.81	0.09	2.07	0.91	2.64	48
n = 3	*SD*	*0.06*	*0.06*	*0.04*	*0.01*	*0.04*	*0.04*	*0.00*	*0.06*	*0.03*	*0.02*	*0.05*	*0.10*	*12*
MG-11′	Mean	3.13	0.87	1.80	0.01	0.15	0.09	0.00	0.90	0.07	2.05	0.97	2.67	38
n = 16	*SD*	*0.04*	*0.04*	*0.03*	*0.01*	*0.02*	*0.03*	*0.00*	*0.04*	*0.02*	*0.02*	*0.04*	*0.06*	*8*
MG-7	Mean	3.21	0.79	1.61	0.02	0.26	0.17	0.01	0.98	0.03	2.06	1.02	2.40	40
n = 10	*SD*	*0.02*	*0.02*	*0.02*	*0.01*	*0.03*	*0.02*	*0.01*	*0.02*	*0.03*	*0.02*	*0.03*	*0.03*	4
Beni Mezala 2														
MG-61	Mean	3.15	0.85	1.78	0.01	0.14	0.11	0.00	0.97	0.04	2.05	1.01	2.63	45
n = 11	*SD*	*0.02*	*0.02*	*0.02*	*0.01*	*0.03*	*0.01*	*0.00*	*0.03*	*0.01*	*0.01*	*0.03*	*0.02*	*6*
MG-62	Mean	3.18	0.82	1.71	0.02	0.22	0.13	0.00	0.91	0.05	2.08	0.97	2.53	37
n = 15	*SD*	*0.03*	*0.03*	*0.02*	*0.00*	*0.02*	*0.01*	*0.00*	*0.04*	*0.01*	*0.01*	*0.04*	*0.04*	*2*
Beni Mezala 1														
MG-19	Mean	3.25	0.75	1.76	0.01	0.04	0.21	0.00	0.93	0.04	2.03	0.97	2.50	83
n = 12	*SD*	*0.02*	*0.02*	*0.02*	*0.00*	*0.00*	*0.02*	*0.00*	*0.03*	*0.02*	*0.02*	*0.04*	*0.03*	*2*
MG-18	Mean	3.31	0.69	1.63	0.02	0.14	0.28	0.00	0.85	0.03	2.07	0.89	2.32	65
n = 16	*SD*	*0.06*	*0.06*	*0.07*	*0.01*	*0.04*	*0.06*	*0.00*	*0.05*	*0.02*	*0.03*	*0.05*	*0.12*	*6*
MG-15	Mean	3.12	0.88	1.76	0.02	0.19	0.09	0.00	0.81	0.15	2.07	0.96	2.64	32
n = 21	*SD*	*0.03*	*0.03*	*0.03*	*0.00*	*0.02*	*0.02*	*0.00*	*0.03*	*0.04*	*0.01*	*0.03*	*0.06*	*5*
MG-14	Mean	3.07	0.93	1.88	0.02	0.13	0.04	0.00	0.74	0.17	2.07	0.91	2.81	19
n = 6	*SD*	*0.03*	*0.03*	*0.06*	*0.02*	*0.04*	*0.04*	*0.01*	*0.05*	*0.06*	*0.03*	*0.07*	*0.08*	*17*
RMG-13D f	Mean	3.15	0.85	1.80	0.01	0.15	0.10	0.01	0.77	0.12	2.07	0.90	2.65	40
n = 6	*SD*	*0.02*	*0.02*	*0.02*	*0.00*	*0.01*	*0.02*	*0.01*	*0.06*	*0.03*	*0.02*	*0.05*	*0.02*	*3*
MG-12	Mean	3.17	0.83	1.70	0.02	0.21	0.14	0.00	0.96	0.04	2.07	1.00	2.53	40
n = 7	*SD*	*0.04*	*0.04*	*0.10*	*0.01*	*0.08*	*0.04*	*0.00*	*0.03*	*0.02*	*0.02*	*0.02*	*0.14*	*5*
MG-63	Mean	3.13	0.87	1.76	0.02	0.18	0.10	0.00	0.93	0.06	2.07	0.99	2.63	36
n = 16	*SD*	*0.04*	*0.04*	*0.06*	*0.01*	*0.05*	*0.03*	*0.00*	*0.03*	*0.03*	*0.02*	*0.02*	*0.10*	*4*
MG-64	Mean	3.15	0.85	1.72	0.01	0.20	0.12	0.00	0.96	0.04	2.05	1.01	2.57	36
n = 20	*SD*	*0.03*	*0.03*	*0.03*	*0.00*	*0.03*	*0.02*	*0.00*	*0.02*	*0.02*	*0.01*	*0.02*	*0.04*	*4*
MG-65	Mean	3.14	0.86	1.76	0.02	0.18	0.10	0.00	0.94	0.04	2.06	0.98	2.62	36
n = 10	*SD*	*0.02*	*0.02*	*0.04*	*0.01*	*0.03*	*0.02*	*0.00*	*0.02*	*0.02*	*0.01*	*0.02*	*0.05*	*7*

n: number of the measured grains; *SD:* standard deviation (with italic); Σ oct.: sum of octahedral cations; Σ inter.: sum of the interlayer cations; $Al^t = {}^{IV}Al + {}^{VI}Al$; $\#Mg = [Mg/(Mg + Fe^{2+})] \times 100$.

Table 5. Selected structural formulae for intermediate white micas and paragonite from Federico phyllites normalized to $O_{10}(OH)_2$.

Unit/Sample	Si	^{IV}Al	^{VI}Al	Ti	Fe^{2+}	Mg	Ca	K	Na	Σ Oct.	Σ Inter.	Al^t	#Mg	#Na
Boquete Anjera														
SEM data														
MG-23f C.2.2.1 4	2.95	1.05	1.92	0.01	0.10	0.03	0.09	0.34	0.46	2.07	0.89	2.97	25	57
MG-23f P 20	3.06	0.94	1.95	0.01	0.08	0.01	0.05	0.25	0.47	2.08	0.77	2.89	14	65
MG-23f C.3.1 2	3.08	0.92	1.90	0.01	0.07	0.04	0.05	0.54	0.30	2.03	0.89	2.82	35	36
AEM data														
MG-21 1k TEM	2.92	1.08	1.89		0.11	0.09	0.00	0.58	0.34	2.09	0.92	2.97	45	37
MG-21 5k TEM	3.00	1.00	2.01		0.00	0.05	0.00	0.29	0.57	2.06	0.86	3.01	100	66
MG-21 11 TEM	3.24	0.76	1.69		0.14	0.12	0.00	0.33	0.73	1.95	1.06	2.45	46	69
MG-21 9 TEM	3.08	0.92	1.65		0.23	0.14	0.07	0.09	0.81	2.02	0.97	2.57	38	90
MG-21 10 TEM	3.17	0.83	1.66		0.20	0.09	0.09	0.11	0.85	1.95	1.05	2.49	31	89
Beni Mezala 1														
SEM data														
MG-15 C.7.1 1	2.97	1.03	1.93	0.01	0.08	0.04	0.06	0.27	0.56	2.06	0.89	2.96	32	67
MG-15 C.5.1.1.1 1	3.08	0.92	1.86	0.01	0.15	0.04	0.02	0.57	0.35	2.06	0.94	2.78	23	38
MG-14 51PM	2.76	1.24	2.01	0.00	0.01	0.00	0.19	0.22	0.66	2.04	1.07	3.25	0	75
MG-14 53PM	3.16	0.84	1.90	0.00	0.06	0.03	0.00	0.58	0.33	2.04	0.91	2.74	36	36
MG-14 48PM	2.61	1.39	2.03	0.01	0.05	0.05	0.33	0.03	0.48	2.15	0.83	3.42	53	95
MG-14 50PM	2.70	1.30	2.00	0.02	0.04	0.00	0.23	0.08	0.69	2.09	1.00	3.30	0	90
MG-14 45PM	2.89	1.11	1.99	0.00	0.02	0.05	0.14	0.08	0.68	2.07	0.90	3.10	71	89
MG-14 C.3 1	2.80	1.20	2.00	0.00	0.04	0.00	0.14	0.06	0.79	2.04	0.99	3.20	0.00	93
AEM data														
MG-14 12 TEM	2.92	1.08	1.77		0.15	0.12	0.00	0.73	0.37	2.04	1.10	2.85	44	34
MG-14 15 TEM	3.16	0.84	1.75		0.14	0.14	0.00	0.56	0.36	2.03	0.92	2.59	50	39

Σ oct.: sum of octahedral cations; Σ inter.: sum of the interlayer cations; $Al^t = {}^{IV}Al + {}^{VI}Al$; $\#Mg = [Mg/(Mg + Fe^{2+})] \times 100$; $\#Na = [Na/(Na + K + Ca)] \times 100$.

Table 6. Selected structural formulae of K-rich dioctahedral micas from detrital-like crystals from ghomaride sandstone and Federico quartzites obtained by SEM/EDX and normalized to $O_{10}(OH)_2$.

Unit	Si	^{IV}Al	^{VI}Al	Ti	Fe^{2+}	Mg	Ca	K	Na	Σ Oct.	Σ Inter.	Al^t	#Mg
Ghomaride complex													
Koudiat Tiziane unit													
MG-40 C1 1	3.10	0.90	1.90	0.02	0.05	0.08	0.00	0.75	0.10	2.05	0.85	2.80	61
MG-40 SC3Z1B 2	3.11	0.89	1.81	0.04	0.06	0.09	0.00	0.84	0.12	2.02	0.96	2.70	59
MG-40 C7Z1 5	3.12	0.88	1.91	0.00	0.04	0.06	0.00	0.95	0.00	2.01	0.95	2.79	58
MG-40 SC3Z1 4	3.15	0.85	1.78	0.04	0.09	0.10	0.00	0.89	0.09	2.01	0.98	2.63	54
MG-40 C5Z3 1	3.16	0.84	1.77	0.02	0.12	0.13	0.00	0.83	0.12	2.04	0.95	2.61	51
MG-40 C7Z1 4	3.19	0.81	1.91	0.00	0.00	0.09	0.00	0.90	0.00	2.00	0.90	2.72	100
MG-40 SC3Z1 3	3.20	0.80	1.80	0.03	0.05	0.14	0.02	0.78	0.10	2.01	0.91	2.60	74
MG-40 C5Z3B 4	3.20	0.80	1.73	0.02	0.15	0.15	0.00	0.90	0.04	2.05	0.94	2.54	50
MG-40 C5Z3B 5	3.22	0.78	1.72	0.02	0.14	0.16	0.00	0.88	0.05	2.04	0.93	2.50	53
Federico units													
Beni Mezala 2													
MG-61 4d	3.07	0.93	1.84	0.03	0.10	0.06	0.00	0.88	0.11	2.02	0.99	2.77	36
MG-61 5d	3.35	0.65	1.63	0.02	0.15	0.25	0.00	0.94	0.01	2.05	0.95	2.28	63
MG-61 6d	3.36	0.64	1.61	0.02	0.16	0.28	0.00	0.92	0.02	2.06	0.94	2.25	64
Beni Mezala 1													
MG-19 13d	3.35	0.65	1.70	0.02	0.07	0.24	0.01	0.85	0.06	2.03	0.92	2.36	77
MG-12 26d	3.08	0.92	1.90	0.02	0.07	0.04	0.00	0.86	0.10	2.03	0.96	2.83	39
MG-12 27d	3.19	0.81	1.62	0.02	0.30	0.15	0.00	1.01	0.01	2.09	1.02	2.43	34
MG-12 28d	3.23	0.77	1.66	0.01	0.23	0.16	0.00	0.97	0.01	2.08	0.98	2.43	40

Σ oct.: sum of octahedral cations; Σ inter.: sum of the interlayer cations; $Al^t = {}^{IV}Al + {}^{VI}Al$; $\#Mg = [Mg/(Mg + Fe^{2+})] \times 100$.

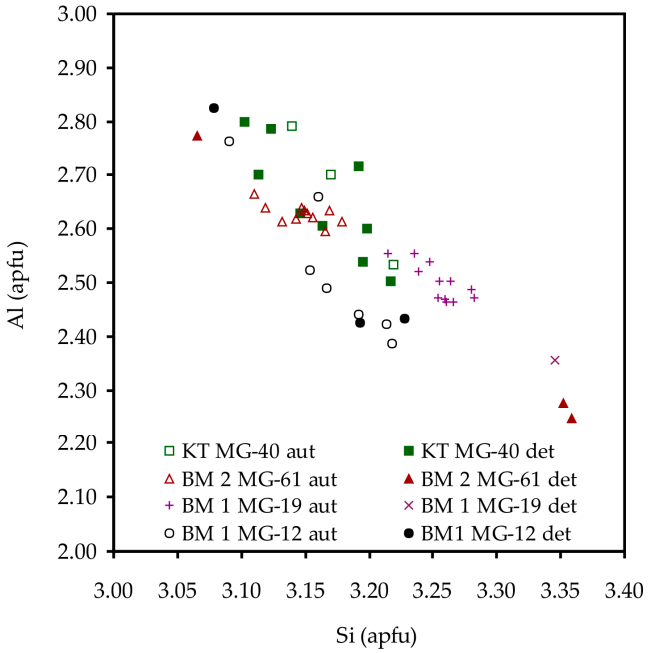

Figure 15. Si vs. Al contents of detrital and authigenic white micas from ghomaride and federico samples. Solid symbols: detrital micas; open symbols: authigenic micas.

4.5.2. Chlorites

The trioctahedral chlorites, which have an Fe/(Fe + Mg) ratio <0.3, correspond mainly to the clinochlore (Mg-rich) variety (Table 7). Very small amounts of K, Na, and Ca have been found, thought to be the result of contamination by dioctahedral micas as a result of the fine intergrowths of these phyllosilicates in the studied rocks or by the presence of isolated layers of micas inside the chlorites packets (Figure 11c). In addition, some analyses of these phyllosilicates in Beni Mezala samples are characterized by a sum of octahedral cations around 5.5 *apfu* and a Si content higher than 3 *apfu*. In these analyses, total Fe was considered as Fe^{2+} although the sum of octahedral cations could suggest a major presence of Fe^{3+} according to Fransolet and Bourguignon [57]. However, considering the TEM data (Figure 10b), most likely, these analyses are the result of contamination by vermiculite layers. With respect to sudoites, these di-trioctahedral chlorites were identified in Ghomaride complex and Tizgarine unit, but the analyses are not shown due to the high grade of contamination by alkali elements, probably due, as in the case of clinochlore, to the presence of mica layers.

4.5.3. Other Phyllosilicates

The composition of kaolinite from ghomaride samples (Table 8) shows a high Al content, with minor quantities of alkaline elements as a consequence of the contamination with illite. In general, the kaolinite analyzed in Tizgarine unit is pure.

Pyrophyllite was only analyzed in the Tizgarine unit. It has an Al-rich composition and low interlaminar occupation (Table 8), maybe due also to contamination with illite.

Table 7. Representative structural formulae of chlorites and mixed-layer chlorite/vermiculite from Federico samples normalized to $O_{10}(OH)_8$.

Mineral/Unit/Sample	Si	^{IV}Al	^{VI}Al	Ti	Fe^{2+}	Mg	Ca	K	Na	Σ Oct.	Σ Inter.	Al^t	#Mg
Chlorite													
Boquete Anjera/SEM data													
MG-21 3.2 14	2.72	1.28	1.43	0.01	1.02	3.42	0.00	0.01	0.05	5.90	0.06	2.72	77
MG-11′ 1.7 25	2.67	1.33	1.47	0.00	0.90	3.55	0.00	0.00	0.00	5.93	0.00	2.80	80
MG-11′ 3.3 29	2.70	1.30	1.47	0.00	0.88	3.57	0.00	0.00	0.00	5.92	0.00	2.77	80
MG-11′ 3.4 33	2.73	1.27	1.52	0.00	0.91	3.41	0.00	0.00	0.00	5.88	0.00	2.79	79
Boquete Anjera/AEM data													
MG-21 AEM/TEM	2.63	1.37	1.64	0.00	0.59	3.39	0.00	0.05	0.00	5.62	0.05	3.01	85
MG-21 AEM/TEM	2.64	1.36	1.54	0.00	0.67	3.43	0.00	0.05	0.00	5.63	0.05	2.90	84
Beni Mezala 2/SEM data													
MG-62 5.2.2	2.71	1.29	1.32	0.00	1.12	3.49	0.00	0.01	0.02	5.95	0.03	2.60	76
MG-62 5.1.2	2.73	1.27	1.33	0.00	1.17	3.45	0.00	0.00	0.02	5.96	0.02	2.61	75
MG-62 5.2.1	2.80	1.20	1.44	0.00	1.05	3.40	0.00	0.02	0.00	5.89	0.02	2.64	76
Beni Mezala 1/SEM data													
MG-15 5.1.3.2	2.68	1.32	1.41	0.00	1.93	2.56	0.00	0.01	0.06	5.92	0.07	2.74	57
MG-15 6.2.3	2.67	1.33	1.40	0.00	1.90	2.63	0.01	0.01	0.03	5.94	0.05	2.73	58
MG-15 1.1-2.2	2.71	1.29	1.32	0.00	2.03	2.53	0.02	0.01	0.00	5.94	0.02	2.61	56
MG-14 P 4	2.45	1.55	1.55	0.00	1.01	3.49	0.01	0.04	0.00	6.05	0.05	3.10	78
MG-14 3b.3	2.64	1.36	1.37	0.00	1.02	3.57	0.00	0.00	0.00	5.99	0.00	2.73	78
MG-14 4.3.5	2.72	1.28	1.47	0.00	0.97	3.42	0.00	0.00	0.05	5.88	0.05	2.76	78
MG-14 P27	2.86	1.14	1.74	0.01	1.00	3.06	0.00	0.00	0.00	5.81	0.00	2.88	75
MG-65 43	2.88	1.12	1.32	0.00	1.40	3.23	0.01	0.00	0.00	5.98	0.01	2.44	70
Beni Mezala 1/AEM data													
MG-14 AEM/TEM	2.71	1.29	1.56	0.00	0.90	3.06	0.00	0.00	0.00	5.52	0.00	2.85	77
Mixed layer Chlorite/Vermiculite													
Beni Mezala 2/SEM data													
MG-62 1.3.1.1	3.19	0.81	1.71	0.00	1.51	2.26	0.02	0.01	0.01	5.50	0.04	2.52	60
MG-62 1.1.2.3	3.21	0.79	1.66	0.01	1.61	2.27	0.03	0.01	0.00	5.56	0.04	2.45	58
Beni Mezala 1/SEM data													
MG-18 M1.3.2	3.21	0.79	1.50	0.00	0.79	3.35	0.00	0.00	0.00	5.64	0.00	2.29	81
MG-18 M1.3.11	3.11	0.89	1.52	0.00	0.61	3.55	0.00	0.00	0.00	5.68	0.00	2.41	85
MG-63 2.1.1.2	3.17	0.83	1.63	0.00	1.45	2.41	0.00	0.00	0.04	5.49	0.05	2.46	62
MG-63 1.2.2	3.26	0.74	1.67	0.01	1.54	2.24	0.00	0.01	0.04	5.45	0.05	2.40	59

Σ oct.: sum of octahedral cations; Σ inter.: sum of the interlayer cations; $Al^t = {}^{IV}Al + {}^{VI}Al$; #Mg = $[Mg/(Mg + Fe^{2+})] \times 100$.

Table 8. Average structural formulae of kaolinite and pyrophyllite from samples normalized to $O_{10}(OH)_8$ and $O_{10}(OH)_2$, respectively. Fe calculated as Fe^{3+}.

Unit/Sample		Si	^{IV}Al	^{VI}Al	Ti	Fe^{3+}	Mg	Ca	K	Na	Σ Oct.	Σ Inter.	Al^t
Kaolinite													
Ghomaride complex													
Beni Hozmar/BH-3	Mean	3.98	0.03	3.93	0.00	0.01	0.02	0.01	0.09	0.02	3.96	0.11	3.97
n = 12	*SD*	0.05	0.03	0.07	0.01	0.01	0.02	0.01	0.08	0.02	0.05	0.09	0.09
Aakaili/MG-56	Mean	3.98	0.03	3.89	0.00	0.03	0.10	0.00	0.04	0.04	4.01	0.08	3.92
n = 6	*SD*	0.04	0.02	0.08	0.00	0.02	0.10	0.00	0.03	0.03	0.05	0.06	0.08
Federico units													
Tizgarine/MG-34	Mean	4.11	0.00	3.83	0.00	0.01	0.01	0.01	0.00	0.00	3.85	0.01	3.83
n = 3	*SD*	0.09	0.00	0.10	0.00	0.01	0.01	0.01	0.00	0.00	0.12	0.01	0.10
Pyrophyllite													
Federico units													
Tizgarine/MG-34	*Mean*	3.93	0.09	1.98	0.00	0.01	0.01	0.00	0.04	0.01	2.00	0.06	2.07
n = 7	*SD*	0.09	0.07	0.07	0.00	0.01	0.01	0.00	0.03	0.02	0.07	0.05	0.13

n: number of the measured grains; *SD:* standard deviation (with italic); Σ oct.: sum of octahedral cations; Σ inter.: sum of the interlayer cations; $Al^t = {}^{IV}Al + {}^{VI}Al$.

4.6. Chlorite Thermometry

Semi-empirical thermometry was applied in samples studied by electron microscopy after a selection of the analyses according to the criteria related to the Si content and the value of octahedral vacancies given by Bourdelle et al. [15] and Lanari et al. [16]. Finally, only analyses from four samples of the Federico units (two from Boquete Anjera unit, one from Beni Mezala 2 unit, and one from Beni

Mezala 1 unit) were valid for the calculations. The Lanari geothermometry calculations were done considering a *P* from 1 to 3 kbar in function of the crystal-chemical parameters determined in the micas of the selected samples. As the values obtained from the different pressures are very similar, the data presented here correspond to the average pressure (2 kbar). The average temperature of each sample with the standard deviation (*SD*) are listed in Table 9, except for sample MG-62, that gives significant differences between the two values obtained (387 and 245 °C according to Bourdelle et al. [15] thermometer and 508 and 254 °C, respectively, with the Lanari et al. [16] thermometer). The temperature estimations of the studied rocks with both the Bourdelle et al. [15] and Lanari et al. [16] approaches are rather similar (Figure 16). Temperatures range between 250 and 400 °C in samples from the Boquete Anjera unit and between 150 and 350 °C in Beni Mezala 1 unit. In any case, the predominant values are higher than 300 °C (Figure 16), which is in coherence with the CIS values of epizone obtained for these units (Figure 5).

Table 9. Summary of temperatures (°C) calculated in chlorites with semi-empirical methods.

Tectonic Units	**Boquete Anjera Unit**		**Beni Mezala 1 Unit**
Samples	MG-21	MG-11′	MG-14
Thermometry			
Bourdelle et al. [15]	289 ± 42	319 ± 31	253 ± 59
Lanari et al. [16]	361 ± 37	331 ± 42	254 ± 62
	n = 2	n = 9	n = 17

Notes: errors are expressed at SD level and numbers of analyses are signaled with "n".

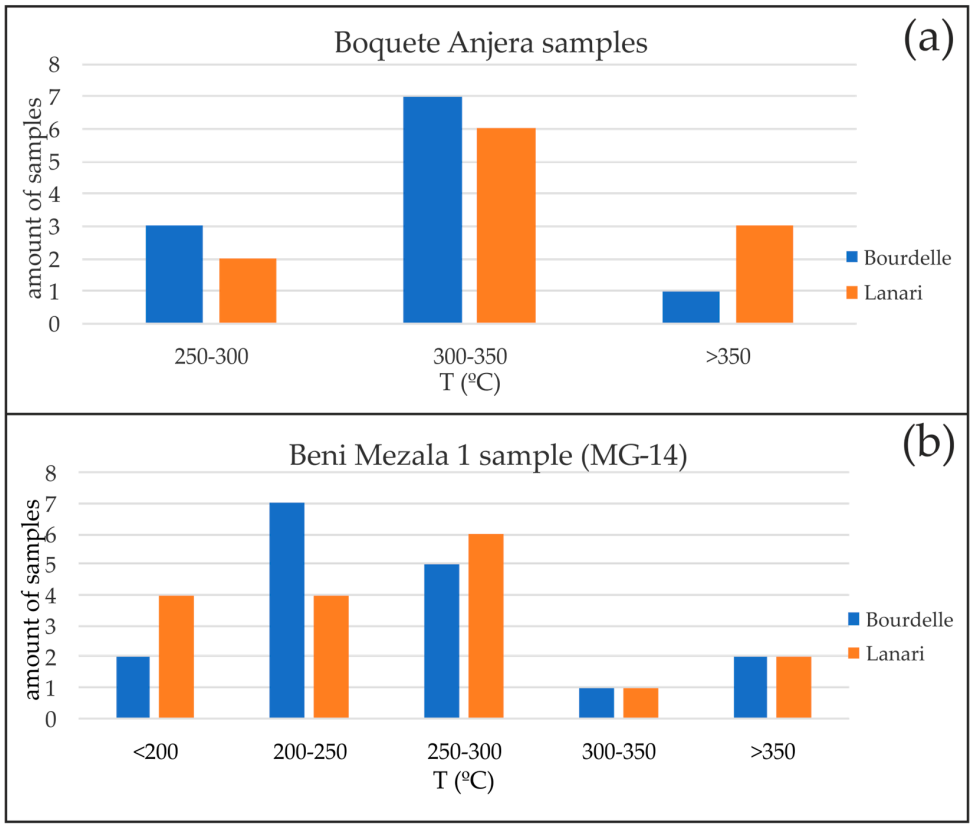

Figure 16. Histograms showing the geothermometric data based on semi-empirical thermometers [15,16] for the deepest intermediate units: (**a**) temperatures obtained for the Boquete Anjera samples (MG-21 and MG-11′); (**b**) temperatures obtained for the Beni Mezala 1 sample (MG-14).

5. Discussion

The study of the mineral assemblages, crystal-chemical parameters of K-white micas, and chemical characterization of phyllosilicates of the clastic rocks of the Ghomaride complex and Federico units is of relevance to the understanding of the diagenetic-metamorphic evolution of these materials after their deposition during the Permo-Triassic.

The rocks of the studied sector include a large range of diagenesis in the Ghomaride complex, with the illite "crystallinity" defining a trend from a very low-temperature environment to epizonal metamorphism in the deepest Federico units (Figure 5). Nevertheless, the evolution of the illite "crystallinity" is not strictly progressive; rather, it shows an abrupt change at the boundary between the Ghomaride complex and Federico units and another step within the Boquete Anjera unit, close to the boundary with the Tizgarine one, probably due to mechanical contacts between Ghomaride complex and Federico units and between Tizgarine and Boquete Anjera tectonic units (Figure 17). The first one marks the transition from the diagenetic to the anchizone and the second one the transition from the anchizone to the epizonal conditions. In any case, there is undoubtedly a clear increase of illite "crystallinity" with depth and this is in coherence with the mineralogical and textural evolution, as it will be addressed in the following paragraphs.

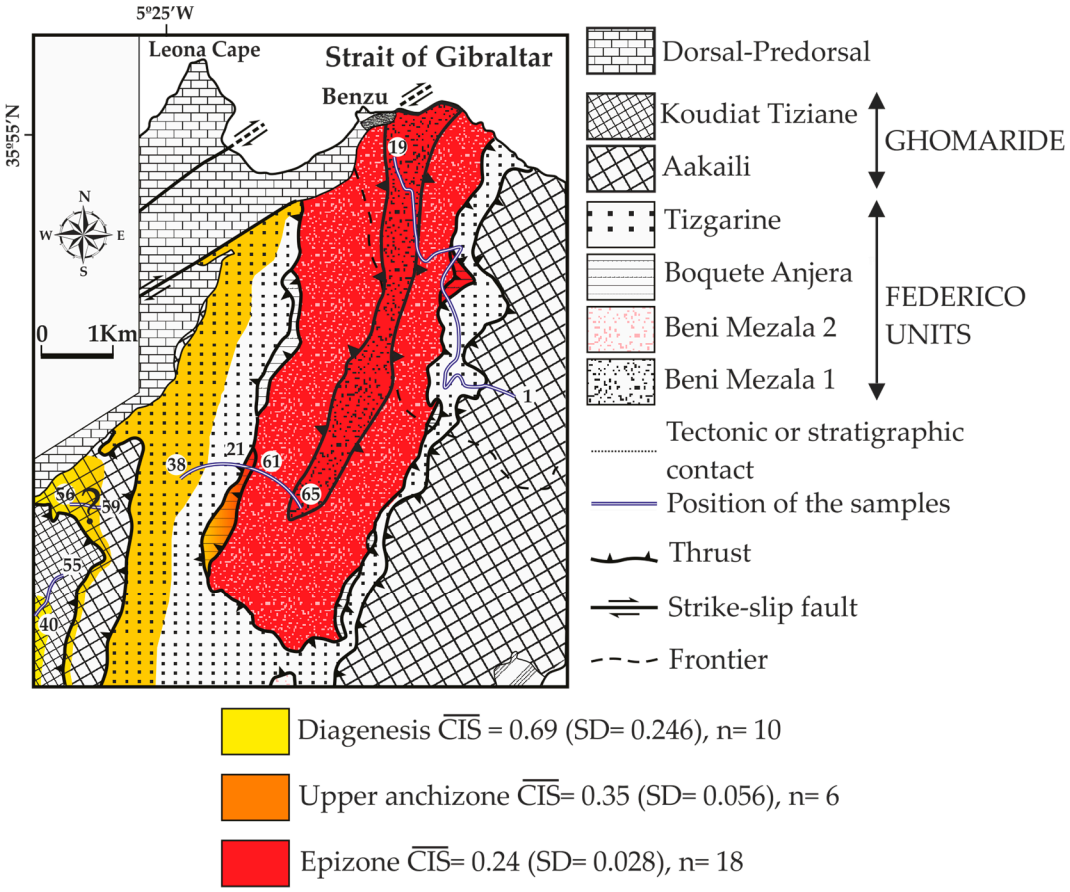

Figure 17. Illite "crystallinity" (CIS values) of the studied samples in relation to their geographic position and geological context.

Specifically, the crystal-chemical parameters and mineral assemblages of the ghomaride sandstones established by XRD are similar to the few pelites found in the Ghomaride complex. Obviously, the pelites have a higher proportion of phyllosilicates. However, according to previous works [58,59], although sandstones and pelites can be very different in relation to macroscopic features and mechanical aspects, it is not like that at the nanoscale nor in the chemistry of phyllosilicates. Illite, kaolinite, and

minor quantities of illite/smectite mixed-layers and chlorite are present in the shallowest samples. Other phyllosilicates as dickite and sudoite were also identified in deeper samples with CIS values close to the diagenesis–anchizone boundary, forming, in some cases, intergrowths with illite or a wide variety of mixed-layer structures at the nanoscale. A detailed study about the mechanisms of the formation of kaolinite, dickite, sudoite, and illite in these units have been carried out by Ruiz Cruz et al. [3], where a temperature of ~150 °C is given for the kaolinite-dickite reaction in coherence with the CIS data presented here. Moreover, these clay minerals have also been described in the equivalent units of the Betic Cordillera [3,17,60]. Lastly, in the deepest ones (Aakaili Unit), Na-K mica appears for the first time. The mineral assemblages of the Federico units' samples are characterized by the appearance of an index mineral, pyrophyllite in Tizgarine unit, coinciding with the lower anchizone limit (T ~200 °C) and coexisting with minor dickite, illite-muscovite (K and Na-K), and chlorite (tri- and di-tri). The appearance of pyrophyllite was explained as a transformation of dickite observed in selected Triassic samples from the Betic-Rif Cordillera ([3], Figure 5). Clastic rocks from Boquete Anjera show several differences from the previous ones: the first appearance of paragonite, the presence of true muscovites, and, from the textural point of view, a well-developed slaty cleavage. All these observations coincide with epizone values. These features are also present in the samples corresponding to the deepest unit (Beni Mezala), where Na-Ca mica, talc, vermiculite, chlorite/vermiculite, and kaolinite have been well described sporadically, although the last two mineral phases are not the result of a prograde evolution, as it will be commented later.

The mineral evolution described through the Beni Mezala antiform is a very good example of reaction progress in the frame of the Ostwald-step processes [7]: Metastable clay systems undergoing reactions towards chemical and textural equilibrium, which is almost reached in the epizone samples. The coexistence of illite/smectite mixed-layers and illite small packets in the diagenetic samples, which are substituted by large crystals of muscovite and paragonite in the highest metamorphic grade samples, or the presence of pyrophyllite in Tizgarine unit (lower anchizone), but the absence of kaolinite, fit quite well with the trends previously described by other authors ([8–10]; among others). In this sense, samples in which muscovite, paragonite, and intermediate Na-K mica occur together (Table 2 and Figure 14) are consistent with metastability, not only because more than two such micas appear but also because their compositions are incompatible with the solvus in the muscovite-paragonite system [61,62]. The existence of true intermediate Na-K mica was already demonstrated by TEM/AEM studies [61,63], although later, Livi et al. [64] proposed the nano-domain model, which supposes that clay minerals may contain a wide range of cations mixed non-homogeneously within an interlayer at low temperatures. Finally, in relation to the mica polytypism, the most common polytype in the studied samples is the $2M_1$, which is typical of metamorphic micas, but the 1M polytype occurs also in some diagenetic samples (Ghomaride complex) and the 3T polytype in some epizone samples. The appearance of different mica polytypes is also indicative of a lack of equilibrium. The occurrence of minerals that correspond to different conditions and consequently, different times on the PTt (Pressure-Temperature-time) path, giving non-equilibrium mineral assemblages, is a common feature in low-grade metamorphic rocks.

The b cell parameter of dioctahedral micas, ranging from 8.987 to 9.036 Å and roughly increasing from the ghomaride samples to the Federico ones, is also characteristic of low (1–2 kbar) to intermediate (2–3 kbar) pressure regional metamorphism according to Guidotti and Sassi [13]. However, in the deepest Federico units (Boquete Anjera and Beni Mezala units), the presence of 3T mica polytype (Figure 6) and the wide range of phengitic substitution values (Si from 3 up to more than 3.35 *apfu*, Figure 13b) indicates the coexistence of mica grains formed under a wider range of pressure. The detailed research carried out by Ruiz-Cruz et al. [65] about the petrology of the phyllites and the enclosed veins found in the Beni Mezala 1 sequence showed the presence of pumpellyite—actinolite—epidote in the veins from Permo-Triassic formations, indicating pressures of ~2 kbar. This agrees with the estimations deduced from crystal-chemical parameters of white mica (CIS, b) from the enclosing pumpellyite-free phyllites (MG-14 and MG-13, Table 2). Nevertheless, the outstanding presence of kyanite-bearing veins in the same area suggests pressure conditions of 5 kbar [65]. With respect to the temperature

conditions, in addition to the CIS values and the presence of minerals as pyrophyllite (*T* ~200 °C, lower anchizonal limit) and paragonite (anchizone and epizone mineral), semi-empirical chlorite thermometers show results for the deepest Federico units that are coherent with the rest of the data. Temperature ranges are narrower in samples from the Boquete Anjera unit (250–400 °C) than in Beni Mezala 1 unit (150–350 °C), but in any case, these temperature ranges suggest the genesis of several populations of chlorites during the PTt evolution of the orogen as in the case of dioctahedral micas as it is commented below. In relation to the thermal conditions, the enclosed veins found in the Beni Mezala 1 sequence indicate temperatures of ~250 °C and the kyanite-bearing veins in the same area suggest peak conditions of 400 °C [65]. Nevertheless, these estimates in Beni Mezala 1 unit are far from those deduced by Bouybaouène [22] and Bouybaouène et al. [24] based on paragenesis with carpholite and talc, and other data relative to the Betic Cordillera [66].

According to our data, the presence of micas 3*T* is interpreted as being formed during the Alpine episode of high pressure and low temperature (H*P*/L*T*), which implies a collisional regime ([22,24,66,67]; and see [68–70] for a review). Nevertheless, the $2M_1$ micas have to be the result of a rebalancing of part of the first population of micas 3*T* during the highest temperature and lowest pressure episode that characterized the beginning of the exhumation of the orogen. A similar interpretation was made by Frey et al. [52] and Stökhert [53] for explaining the coexistence of these two polytypes of mica in polymetamorphic rocks of the Alps. In this research, the continuous trend observed in mica compositions also corroborates this hypothesis, reflecting the decompression path after the peak pressure. The maximum phengitic values give the pressure of the H*P* episode and the average is coherent with the *b* parameter. A similar reasoning was developed by Abad et al. [71] for the Tien Shan Cordillera. Coherently, the Ghomaride samples show a lower range of phengitic compositions (Figure 12b) and a lower *b* parameter. The large range of diagenesis in the Ghomaride complex, with the CIS data defining a trend from a very low-temperature environment to epizonal metamorphism in the deepest Federico units, just overlying the Sebtide complex, fits with the PTt path established by Azañón and Crespo-Blanc [72] for the Central Betics, resulting in other cases of diagenetic to low-grade metamorphic sequence subject to tectonic stress, which favored the prograde reaction series, instead of burial depth ([17,73], among others).

In relation to the presence of low-*T* mineral phases as chlorite/vermiculite and kaolinite (MG-18, Table 2) in the deepest Federico units, the study of strongly deformed sudoite-bearing synfolial quartz veins present in this whitish schist [74] suggests a retrograde event altering the sudoite to chlorite/vermiculite intergrowth, kaolinite, and minor Fe oxide, probably during the latest stage of exhumation, under low-temperature conditions. This retrograde diagenetic [75] process has been described in both the intermediate units [17,19] and other complexes of the Betic Cordillera [76,77].

Lastly, considering the different positions in the geological literature on the existence or not of intermediate units between the Ghomaride and Sebtide complexes over time ([22,25,30,33,37] and references therein), the mineral data presented here suggest that the transition between Ghomaride and Sebtide complexes is gradual as concluded by Sanz de Galdeano et al. [33]. So, we suggest that the Federico units can be considered intermediate units, and in the case that they were considered the cover of Sebtide complex, it is evident that Tizgarine unit shows more affinity for the ghomaride units than for the deepest Federico ones, as evidenced by the lithological characteristics, the progressive trends of phyllosilicates assemblages, and chemical compositions of the K-white micas.

6. Conclusions

The Beni Mezala antiform is characterized by a complete sequence of clastic rocks ranging from diagenetic (Ghomaride complex) to epizone conditions (Boquete Anjera and Beni Mezala, Federico units) favored by the tectonic stress of the Alpine orogeny. The reaction progress is evidenced through the clay minerals' evolution (mineral phases, CIS values, polytypes, and textural and chemical features).

The identification of different polytypes in micas (1*M*, $2M_1$ in ghomaride samples and $2M_1$, 3*T* in Federico samples) together with the continuous trend observed in the mica composition, with a

wide range of phengitic values, suggests a PTt evolution of the orogen after the peak pressure, which is coherent with the average value given by the *b* parameter (3–1 kbar), reflecting a decompression path. The $2M_1$ micas would be the result of the rebalancing of part of the high *P* population of micas 3*T* (characteristic of the collisional setting) during a subsequent low pressure and high temperature episode, which characterized the beginning of the exhumation of the orogen. The temperature estimates based on index minerals, CIS data, and chlorite geothermometry give ranges from 150 to 400 °C, the highest temperatures in the deepest samples of the Federico units. The chlorite geothermometry also allowed confirmation of the genesis of several populations of chlorite.

Finally, and regarding the results shown in this article, Federico units can be considered intermediate units between the diagenetic Ghomaride complex and the green-schist facies that characterized the Sebtide complex, although under the mineral data presented here Tizgarine unit shows more affinity for the Ghomaride complex than for the deepest Federico units.

Author Contributions: Mª.D.R.-R. conducted field observations and the sampling. M.J.B. prepared samples for different characterizations. M.D.R.-R. performed microscopic observations in petrographic microscope, SEM and TEM. I.A. performed the geothermometric calculations. All the authors participated in the data interpretation from XRD and electron microscopy, discussed the analytical results and prepared the manuscript, figures and tables.

Funding: This research has been funded by Research Project CGL2009-08186 (Spanish Ministry of Education and Science) and PGC2018-094572-B-I00 (MCIU/AEI/FEDER, EU) and Research Groups RNM-199 and RNM-325 of the Junta de Andalucía.

Acknowledgments: We thank J.L. Baldonedo and A. Gómez from the National Electron Microscopy Center of the Complutense University of Madrid and M.M. Abad from the Centro de Instrumentación Científica of the University of Granada for help with HRTEM work. Authors are also grateful to F. Nieto for his suggestions and comments on an early version, to C. Sanz de Galdeano for his lead and helpful in the fieldwork and to M.D. Ruiz-Cruz for her invaluable help in the framework of this investigation. Finally, the critical reviews and helpful comments and suggestions of three anonymous reviewers and the editor (F.J. Molina) have notably improved the quality of the manuscript.

Conflicts of Interest: The authors declare no conflict of interest. The funders had no role in the design of the study; in the collection, analyses, or interpretation of data; in the writing of the manuscript, or in the decision to publish the results.

References

1. Nieto, F. Characterization of coexisting NH_4- and K-micas in very low-grade metapelites. *Am. Mineral.* **2002**, *87*, 205–216. [CrossRef]
2. Do Campo, M.; Nieto, F. Transmission electron microscopy study of the very low-grade metamorphic evolution in Neoproterozoic Pelites of the Puncoviscana Formation (Cordillera Oriental, NW Argentina). *Clay Miner.* **2003**, *38*, 459–481. [CrossRef]
3. Ruiz Cruz, M.D.; Rodríguez, M.D.; Novák, J.K. The illitization of dickite: Chemical and structural evolution of illite from diagenetic to metamorphic conditions. *Eur. J. Mineral.* **2009**, *21*, 361–372. [CrossRef]
4. Do Campo, M.; Collo, G.; Nieto, F. Geothermobarometry of very low-grade metamorphic pelites of the Vendian-Early Cambrian Puncoviscana Formation (NW Argentina). *Eur. J. Mineral.* **2013**, *25*, 429–451. [CrossRef]
5. Bauluz, B.; Nieto, F. Ammonium-bearing micas in very low-grade metapelites: Micro- and nano-texture and composition. *Clay Miner.* **2018**, *53*, 105–116. [CrossRef]
6. Merriman, R.J.; Peacor, D.R. Very low-grade metapelites: Mineralogy, microfabrics and measuring reaction progress. In *Low-Grade Metamorphism*; Frey, M., Robinson, D., Eds.; Blackwell Science: Oxford, UK, 1999; pp. 10–60.
7. Essene, E.J.; Peacor, D.R. Clay mineral thermometry—A critical perspective. *Clays Clay Miner.* **1995**, *43*, 540–553. [CrossRef]
8. Merriman, R.J. Clay minerals and sedimentary basin history. *Eur. J. Mineral.* **2005**, *17*, 7–20. [CrossRef]
9. Árkai, P. Phyllosilicates in very low-grade metamorphism: Transformation to micas. In *Micas: Crystal Chemistry and Metamorphic Petrology*; Monttana, A., Sassi, F.P., Thompson, J.B., Guggenheim, S., Eds.; Reviews in Mineralogy and Geochemistry: Michigan, MI, USA, 2002; Volume 46, pp. 463–478.

10. Ruiz Cruz, M.D. Genesis and evolution of the kaolin-group minerals during the diagenesis and the beginning of metamorphism. In *Diagenesis and Low-Temperature Metamorphism. Theory, Methods and Regional Aspect*; Fernando Nieto, F., Jiménez-Millán, J., Eds.; Seminarios de la Sociedad Española de Mineralogía: Jaén, España, 2007; Volume 3, pp. 41–52.
11. Ali, A. The tectono-metamorphic evolution of the Balcooma Metamorphic Group, north-eastern Australia: A multidisciplinary approach. *J. Metamorph. Geol.* **2010**, *28*, 397–422. [CrossRef]
12. Lanari, P.; Guillot, S.; Schwartz, S.; Vidal, O.; Tricart, P.; Riel, N.; Beyssac, O. Diachronous evolution of the alpine continental subduction wedge: Evidence from P-T estimates in the Briançonnais Zone houillère (France-Western Alps). *J. Geodyn.* **2012**, *56*, 39–54. [CrossRef]
13. Guidotti, C.V.; Sassi, F.P. Classification and correlation of metamorphic facies series by means of muscovite b_0 data from low-grade metapelites. *Neues Jahrb. Mineral. Abh.* **1986**, *153*, 363–380.
14. Kübler, B. Evaluation quantitative du métamorphisme par la cristallinité de l'illite. *Bull. Cent. Rech.* **1968**, *2*, 385–397.
15. Bourdelle, F.; Parra, T.; Chopin, C.; Beyssac, O. A new chlorite geothermometer for diagenetic to low-grade metamorphic conditions. *Contrib. Mineral. Petrol.* **2013**, *165*, 723–735. [CrossRef]
16. Lanari, P.; Wagner, T.; Vidal, O. A thermodinamical model for di-trioctahedral chlorite from experimental and natural data in the system MgO-FeO-Al_2O_3-SiO_2-H_2O: Applications to P-T sections and geothermometry. *Contrib. Mineral. Petrol.* **2014**, *167*, 968. [CrossRef]
17. Abad, I.; Nieto, F.; Peacor, D.R.; Velilla, N. Prograde and retrograde diagenetic and metamorphic evolution in metapelitic rocks of Sierra Espuña (Spain). *Clay Miner.* **2003**, *38*, 1–23. [CrossRef]
18. Lázaro, C.; Ruiz Cruz, M.D.; Sanz de Galdeano, C. Características metamórficas del Triásico Maláguide en las unidades intermedias del sector de Diezma (Sierra Arana, Cordillera Bética). *Boletín Soc. Española Mineral.* **2003**, *26*, 123–136.
19. Ruiz Cruz, M.D.; Sanz de Galdeano, C.; Lázaro, C. Metamorphic evolution of Triassic rocks from the transition zone between the Maláguide and Alpujárride complexes (Betic Cordilleras, Spain). *Eur. J. Mineral.* **2005**, *17*, 81–91. [CrossRef]
20. Ruiz Cruz, M.D.; Franco, F.; Sanz de Galdeano, C.; Novák, J.K. Evidence of contrasting low-grade metamorphic conditions from clay mineral assemblages in Triassic Alpujárride-Maláguide transitional units in the Betic Cordilleras, Spain. *Clay Miner.* **2006**, *41*, 619–636. [CrossRef]
21. Chalouan, A.; Michard, A. The Ghomarides nappes, Rif coastal range, Morocco: A Variscan chip in the Alpine belt. *Tectonics* **1990**, *9*, 1565–1583. [CrossRef]
22. Bouybaouène, M.L. Étude Pétrologique des Metapelites des Sebtides Supérieures, Rif Interne, Maroc: Une Évolution Métamorphique de Haute Pression. Ph.D. Thesis, University of Mohammed V, Rabat, Morocco, 1993.
23. Zaghloul, M.N. Les Unites Federico Septentrionales (Rif Interne, Maroc): Inventaire des Déformations et Contexte Géodynamique dans la Chaîne Bético-Rifaine. Ph.D. Thesis, University of Mohammed V, Rabat, Morocco, 1994.
24. Bouybaouène, M.L.; Goffé, B.; Michard, A. High-pressure, low-temperature metamorphism in the Sebtides nappes, northern Rif, Morocco. *Geogaceta* **1995**, *17*, 117–119.
25. Chalouan, A. Les depots du Trias du Rif interne: Témoins de deux paléomarges téthysiennes en voie d'individualisation. In *Le Permien et le Trias du Maroc: État des Connaissances*; Medina, F., Ed.; Pumag Edit.: Marrekech, Morocco, 1996; pp. 155–179.
26. Goffé, B.; Michard, A.; García-Dueñas, V.; González-Lodeiro, F.; Monié, P.; Campos, J.; Galindo-Zaldívar, J.; Jabaloy, A.; Martínez-Martínez, J.M.; Simancas, J.F. First evidence of high-pressure, low temperature metamorphism in the Alpujárride nappes, Betic Cordillera (SE Spain). *Eur. J. Mineral.* **1989**, *1*, 139–142. [CrossRef]
27. Michard, A.; Goffé, B.; Bouybaouène, M.L.; Saddiqi, O. Late Hercynian-Mesozoic thinning in the Alboran domain: Metamorphic data from the northern Rif, Morocco. *Terra Nova* **1997**, *9*, 171–174. [CrossRef]
28. Martín-Algarra, A.; Messina, A.; Perrone, V.; Russo, S.; Maaté, A.; Martín-Martín, M. A lost realm in the Internal Domains of the Betic-Rif orogen (Spain and Morocco): Evidence from conglomerates and consequences for Alpine geodynamic evolution. *J. Geol.* **2000**, *108*, 447–467. [CrossRef] [PubMed]

29. Anahnah, F. Estructura Profunda de las Cordilleras Alpinas de Marruecos y del Vulcanismo y Cuencas Sedimentarias Neógenas del Rif Oriental: Implicaciones en la Evolución Tectónica Reciente. Ph.D. Thesis, University of Granada, Granada, Spain, 2012.
30. Kornprobst, J. Contribution à l'étude pétrographique et structurale de la zone interne du Rif (Maroc septentrional). *Notes Serv. Géol. Maroc* **1974**, *251*, 256.
31. Mäkel, G.H. The Geology of the Maláguide Complex and its Bearing on the Geodynamic Evolution of the Betic-Rif Orogen (Southern Spain and Northern Morocco). Ph.D. Thesis, Universiteit van Amsterdam, Amsterdam, The Netherlands, 1985.
32. Maaté, A. Etude Géologique de la Couverture Mésozoïqe et Cénozoïque des Unités Ghomarides au Nord de Tétouan (Rif interne, Maroc). Ph.D. Thesis, University of Toulouse III, Toulouse, France, 1984.
33. Sanz de Galdeano, C.; Andreo, B.; García Tortosa, F.J.; López Garrido, A.C. The Triassic palaeogeographic transition between the Alpujarride and Malaguide complexes. Betic-Rif Internal Zone (S Spain, N Morocco). *Palaeogeogr. Palaeocl.* **2001**, *167*, 157–173. [CrossRef]
34. Durand-Delga, M.; Kornprobst, J. Esquisse géologique de la région de Ceuta (Maroc). *Bull. Soc. Géol. Fr.* **1963**, *7*, 1049–1057.
35. Didon, J.; Durand-Delga, M.; Kornprobst, J. Homologies géologiques entre les deux rives du Détroit de Gibraltar. *Bull. Soc. Géol. Fr.* **1973**, *15*, 77–105. [CrossRef]
36. Chalouan, A. Les Nappes Ghomarides (Rif Septentrional, Maroc), un Terain Varisque dans la Chaîne Alpine. Ph.D. Thesis, Louis Pasteur University, Strasbourg, France, 1986.
37. Chalouan, A.; Michard, A.; El Kadiri, K.h.; Negro, F.; Frizon de Lamotte, D.; Soto, J.I.; Saddiqi, O. The Rift Belt. In *Continental Evolution: The Geology of Morocco*; Michard, A., Saddiqi, O., Chalouan, A., Frizon de Lamotte, D., Eds.; Lecture Notes in Earth Sciences; Springer: Berlin, Germany, 2008; Volume 116, pp. 203–302.
38. Sanz de Galdeano, C. *La Zona Interna Bético-Rifeña*; Universidad de Granada: Granada, Spain, 1997.
39. Milliard, Y. Sur l'existence du permien dans le massif paléozoique interne du Rif (Maroc). *C. R. Acad. Sci. II A* **1959**, *249*, 1051–1052.
40. El Adraoul, A.; Aït Brahim, L.; Sanz de Galdeano, C. Fallas de salto en dirección en el Haouz meridional (Complejo de la Dorsal, Rif Interno, N de Tetuán, Marruecos). Comparación con las Béticas (España). *Geogaceta* **2007**, *41*, 71–74.
41. Kornprobst, J.; Durand-Delga, M. Carte géologique du Rif. Sebta. Échelle 1:50000. Feuille NI-30-XIX-4c. *Notes Serv. Géol. Maroc* **1985**, *1985*, 297.
42. Whitney, D.L.; Evans, B.W. Abbreviations for names of rock-forming minerals. *Am. Mineral.* **2010**, *95*, 185–187. [CrossRef]
43. Kisch, H.J. Illite crystallinity; recommendations on sample preparation, X-ray diffraction settings, and interlaboratory samples. *J. Metamorph. Geol.* **1991**, *9*, 665–670. [CrossRef]
44. Warr, L.N.; Rice, H.N. Interlaboratory standardization and calibration of clay mineral crystallinity and crystallite size data. *J. Metamorph. Geol.* **1994**, *12*, 141–152. [CrossRef]
45. Padan, A.; Kisch, H.J.; Shagam, R. Use of the lattice parameter b_0 of dioctahedral illite/muscovite for the characterization of *P/T* gradients of incipient metamorphism. *Contrib. Mineral. Petrol.* **1982**, *79*, 85–95. [CrossRef]
46. Bailey, S.W. Structures of Layer Silicates. In *Crystal Structures of Clay Minerals and their X-ray Identification*; Brindley, G.W., Brown, G., Eds.; Mineralogical Society: London, UK, 1984; Monograph n° 5; pp. 1–124.
47. Pratt, J.H. On the determination of ferrous iron in silicates. *Am. J. Min.* **1894**, *48*, 149–151. [CrossRef]
48. Nieto, F.; Ortega-Huertas, M.; Peacor, D.R.; Arostegui, J. Evolution of illite/smectite from early diagenesis through incipient metamorphism in sediments of the Basque-Cantabrian Basin. *Clays Clay Miner.* **1996**, *44*, 304–323. [CrossRef]
49. Cliff, G.; Lorimer, G.W. The quantitative analysis of thin specimen. *J. Microsc.* **1975**, *103*, 203–207. [CrossRef]
50. Warr, L.N.; Ferreiro Mählmann, R. Recommendations for Kübler Index standardization. *Clay Miner.* **2015**, *50*, 283–286. [CrossRef]
51. Frey, M. Very low-grade metamorphism of clastic sedimentary rocks. In *Low Temperature Metamorphism*; Frey, M., Ed.; Blackie: Glasgow, UK, 1987; pp. 9–58.
52. Frey, M.; Hunziker, J.C.; Jäger, E.; Stern, W.B. Regional distribution of white K-mica polymorphs and their phengite content in the Central Alps. *Contrib. Mineral. Petrol.* **1983**, *83*, 185–197. [CrossRef]

53. Stökhert, B. Compositional control on polymorphism ($2M_1$-$3T$) of phengitic white mica from high pressure parageneses of the Sesia Zone (lower Aosta valley, Western Alps; Italy). *Contrib. Mineral. Petrol.* **1985**, *89*, 52–58. [CrossRef]
54. Sassi, S.P.; Guidotti, C.V.; Rieder, M.; De Pieri, R. On the occurrence of metamorphic $2M_1$ phengites: Some thoughts on polytypism and crystallization conditions of $3T$ phengites. *Eur. J. Mineral.* **1994**, *6*, 151–160. [CrossRef]
55. Taylor, S.R.; McLennan, S.N. *The Continental Crust: Its Composition and Evolution*; Blackwell: Oxford, UK, 1985.
56. Abad, I.; Nieto, F.; Gutiérrez-Alonso, G.; Do Campo, M.; López-Munguira, A.; Velilla, N. Illitic substitution in micas of very-low grade metamorphic clastic rocks. *Eur. J. Mineral.* **2006**, *18*, 59–69. [CrossRef]
57. Fransolet, A.M.; Bourguignon, P. Di/trioctahedral chlorite in quartz veins from the Ardennes, Belgium. *Can. Mineral.* **1978**, *16*, 365–373.
58. Haszeldine, R.S.; Macaulay, C.I.; Marchand, A.; Wilkinson, M.; Graham, C.M.; Cavanagh, A.; Fallick, A.E.; Couples, G.D. Sandstone cementation and fluids in hydrocarbon basins. *J. Geochem. Explor.* **2000**, *69*, 195–200. [CrossRef]
59. Abad, I.; Nieto, F.; Velilla, N. Chemical and textural characterization of diagenetic to low-grade metamorphic phyllosilicates in turbidite sandstones of the South Portuguese Zone: A comparison between metapelites and sandstones. *Schweiz. Miner. Petrog.* **2002**, *82*, 303–324.
60. Ruiz Cruz, M.D.; Sanz de Galdeano, C. Compositional a structural variation of sudoite from the Betic Cordilleras, Spain: A synthesis. *Clays Clay Miner.* **2005**, *53*, 639–652. [CrossRef]
61. Li, G.; Peacor, D.R.; Merriman, R.J.; Roberts, B. The diagenetic to low grade metamorphism evolution of matrix white mica in the system muscovite-paragonite in a mudrock from Central Wales, UK. *Clays Clay Miner.* **1994**, *42*, 369–381. [CrossRef]
62. Livi, K.J.T.; Veblen, D.R.; Ferry, J.M.; Frey, M. Evolution of 2:1 layered silicates in low-grade metamorphosed Liassic shales of Central Switzerland. *J. Metamorph. Geol.* **1997**, *12*, 323–344. [CrossRef]
63. Jiang, W.T.; Peacor, D.R. Formation and modification of metastable intermediate sodium potassium mica, paragonite, and muscovite in hydrothermally altered metabasites from North Wales. *Am. Mineral.* **1993**, *78*, 782–793.
64. Livi, K.J.T.; Christidis, G.E.; Árkai, P.; Veblen, D.R. White mica domain formation: A model for paragonite, margarite, and muscovite formation during prograde metamorphism. *Am. Mineral.* **2008**, *93*, 520–527. [CrossRef]
65. Ruiz Cruz, M.D.; Sanz de Galdeano, C.; Álvarez-Valero, A.; Rodríguez Ruiz, M.D.; Novák, J. Pumpellyite and coexisting minerals in metapelites and veins from the Federico units in the Internal Zone of the Rif, Spain. *Can. Mineral.* **2010**, *48*, 183–203. [CrossRef]
66. Azañón, J.M.; Goffé, B. Ferro- and magnesiocarpholite assemblages as record of hig-P, low-T metamorphic evolution of the Alpujarride complex in the central Betics (Alboran Domain, SE Spain). *Eur. J. Mineral.* **1997**, *9*, 1035–1051. [CrossRef]
67. Azañón, J.M.; García-Dueñas, V.; Goffé, B. Exhumation of high-pressure metapelites and coeval crustal extension in the Alpujárride complex. *Tectonophysics* **1998**, *285*, 231–252. [CrossRef]
68. Michard, A.; Negro, F.; Saddiqi, O.; Bouybaouène, M.L.; Chalouan, A.; Montigny, R.; Goffé, B. Pressure-temperature-time constraints on the Maghrebide mountain building: Evidences from the Rif-Betic transect (Morocco, Spain), Algerian correlations, and geodynamic implications. *C. R. Geosci.* **2006**, *338*, 92–114. [CrossRef]
69. Vergés, J.; Fernàndez, M. Tethys-Atlantic interaction along the Iberia-Africa plata bounary: The Betic-Rif orogenic system. *Tectonophysics* **2012**, *579*, 144–172. [CrossRef]
70. Platt, J.P.; Behr, W.M.; Johanesen, K.; Williams, J.R. The Betic-Rif Arc and Its Orogenic Hinterland: A Review. *Annu. Rev. Earth Planet. Sci.* **2013**, *41*, 313–357. [CrossRef]
71. Abad, I.; Gutiérrez-Alonso, G.; Nieto, F.; Gertner, I.; Becker, A.; Cabero, A. The structure and the phyllosilicates (Chemistry, crystallinity and texture) of Talas Ala-Tau (Tien-Shan, Kyrgyz Republic): Comparison with more recent subduction complexes. *Tectonophysics* **2003**, *365*, 103–127. [CrossRef]
72. Azañón, J.M.; Crespo-Blanc, A. Exhumation during a continental collision inferred from the tectonometamorphic evolution of the Alpujarride Complex in the cetral Betics (Alboran Domain, SE Spain). *Tectonics* **2002**, *19*, 549–565. [CrossRef]

73. Johnson, M.R.W.; Oliver, G.J.H. Precollision and postcollision thermal events in the Himalaya. *Geology* **1990**, *18*, 753–756. [CrossRef]
74. Ruiz Cruz, M.D.; Rodríguez Ruiz, M.D.; Sanz de Galdeano, C. Stress-induced alteration of sudoite: Structural and chemical modifications. *Clays Clay Miner.* **2010**, *58*, 21–36. [CrossRef]
75. Nieto, F.; Mata, M.P.; Bauluz, B.; Giorgetti, G.; Árkai, P.; Peacor, D.R. Retrograde diagenesis, a widespread process on a regional scale. *Clay Miner.* **2005**, *40*, 93–104. [CrossRef]
76. Orozco, M.; Alonso-Chaves, F.M.; Nieto, F. Development of large north-facing folds and their relation to crustal extension in the Alboran domain (Alpujarras region, Betic Cordilleras, Spain). *Tectonophysics* **1998**, *298*, 271–295. [CrossRef]
77. Nieto, F.; Velilla, N.; Peacor, D.R.; Ortega Huertas, M. Regional retrograde alteration of sub-greenschist facies chlorite to smectite. *Contrib. Mineral. Petrol.* **1994**, *115*, 243–252. [CrossRef]